Stem Cell Reports
Resource
ISSCR
OPEN ACCESS

A defined roadmap of radial glia and astrocyte differentiation from human pluripotent stem cells

Vukasin M. Jovanovic,[1,*] Claire Weber,[1] Jaroslav Slamecka,[1] Seungmi Ryu,[1] Pei-Hsuan Chu,[1] Chaitali Sen,[1] Jason Inman,[1] Juliana Ferreira De Sousa,[1] Elena Barnaeva,[1] Marissa Hirst,[2] David Galbraith,[2] Pinar Ormanoglu,[1] Yogita Jethmalani,[1] Jennifer Colon Mercado,[3] Sam Michael,[1] Michael E. Ward,[3] Anton Simeonov,[1] Ty C. Voss,[1] Carlos A. Tristan,[1] and Ilyas Singeç[1,*]

[1]National Center for Advancing Translational Sciences (NCATS), Division of Preclinical Innovation, Stem Cell Translation Laboratory (SCTL), National Institutes of Health, Rockville, MD 20850, USA
[2]Rancho Biosciences, San Diego, CA 92127, USA
[3]Inherited Neurodegenerative Disease Unit, National Institute of Neurological Disorders and Stroke (NINDS), National Institutes of Health, Bethesda, MD 20892, USA
*Correspondence: vukasin.jovanovic@nih.gov (V.M.J.), ilyassingec@gmail.com (I.S.)
https://doi.org/10.1016/j.stemcr.2023.06.007

SUMMARY

Human gliogenesis remains poorly understood, and derivation of astrocytes from human pluripotent stem cells (hPSCs) is inefficient and cumbersome. Here, we report controlled glial differentiation from hPSCs that bypasses neurogenesis, which otherwise precedes astrogliogenesis during brain development and *in vitro* differentiation. hPSCs were first differentiated into radial glial cells (RGCs) resembling resident RGCs of the fetal telencephalon, and modulation of specific cell signaling pathways resulted in direct and stepwise induction of key astroglial markers (NFIA, NFIB, SOX9, CD44, S100B, glial fibrillary acidic protein [GFAP]). Transcriptomic and genome-wide epigenetic mapping and single-cell analysis confirmed RGC-to-astrocyte differentiation, obviating neurogenesis and the gliogenic switch. Detailed molecular and cellular characterization experiments uncovered new mechanisms and markers for human RGCs and astrocytes. In summary, establishment of a glia-exclusive neural lineage progression model serves as a unique serum-free platform of manufacturing large numbers of RGCs and astrocytes for neuroscience, disease modeling (e.g., Alexander disease), and regenerative medicine.

INTRODUCTION

Neuroglia were first described by Rudolf Virchow in 1846 as a connective substance, or "brain glue," that appeared to surround the nervous elements. Ramón y Cajal predicted the importance of astrocytes and dedicated a significant body of work to their morphological characterization (Garcia-Marin et al., 2007). Astrocytes, the most abundant cell type in the central nervous system (CNS), control structural and functional properties of the human brain (e.g., blood-brain barrier, neurotrophic support, synaptogenesis, synaptic pruning, neurotransmitter uptake, ionic milieu control in the extracellular space, innate and adaptive immunity, neural repair, and others) (Liddelow et al., 2017; Rowitch and Kriegstein, 2010; Verkhratsky and Kettenmann, 1996; Wilton et al., 2019). Impairment of these functions can contribute to disorders such as autism, epilepsy, Alzheimer's disease, amyotrophic lateral sclerosis, and others (Molofsky et al., 2012; Sloan and Barres, 2014; Zuchero and Barres, 2015).

During CNS development, early neuroepithelial cells give rise to RGCs, which generate large numbers of neurons in the cortical plate and provide a glial scaffold for migratory neurons (neurogenic phase) (Noctor et al., 2001; Schmechel and Rakic, 1979). After the progressive waves of neurogenesis, RGCs differentiate into astrocytes and then, later, into oligodendrocytes (gliogenic phase) (Deneen et al., 2006; Hirabayashi et al., 2009; Naka et al., 2008; Rowitch and Kriegstein, 2010). The invariance of this sequence, neurogenesis followed by gliogenesis, is highly conserved throughout vertebrate phylogeny (Deneen et al., 2006). Despite an improved understanding of the spatiotemporal gene-regulatory networks controlling CNS morphogenesis, little is known about the precise cell-intrinsic mechanisms and extracellular signals that coordinate the genesis of human RGCs and their differentiation into astrocytes.

Previous reports generated astrocytes from hPSCs by prolonged culture for 6 months and longer, which seemed necessary to recapitulate the neurogenic-to-gliogenic fate switch (Krencik et al., 2011; Sloan et al., 2017; Velasco et al., 2019). These strategies often required fetal bovine serum (FBS) and cell sorting approaches to enrich for astrocyte-like cells (Leventoux et al., 2020; Sloan et al., 2017; Tcw et al., 2017). Moreover, to accelerate the onset of astrocyte differentiation, recent reports ectopically expressed specific transcription factors in fibroblasts and induced pluripotent stem cell (iPSC)-derived neural stem cells (NSCs) (Caiazzo et al., 2015; Canals et al., 2018). Here, we developed a differentiation method that follows the principles of developmental biology that is stepwise and controlled but also scalable and efficient, as required for clinical applications. We first defined conditions for generation of human RGCs, a cell type that is largely

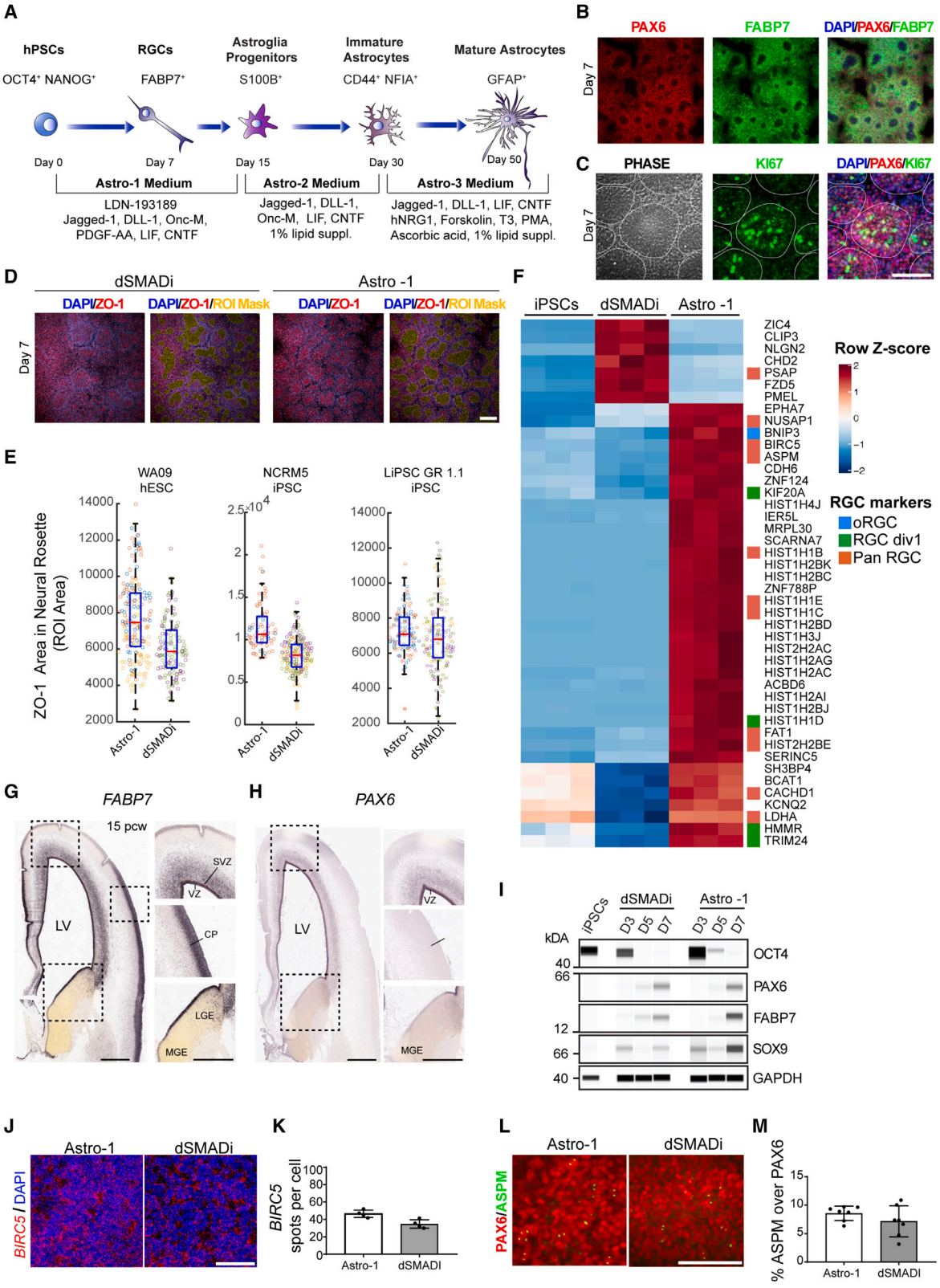

(legend on next page)

understudied. These pure cultures of RGCs were then coaxed exclusively into astrocytes without going through an obligated neurogenic phase. Using this efficient strategy and a robotic cell culture system, we were able to manufacture astrocytes at industrial scale and present a versatile resource to elucidate human glial biology.

RESULTS

Efficient conversion of hPSCs into RGCs

All experiments described here were performed using human embryonic stem cell (hESC) and iPSC lines that were continuously cultured under feeder-free, chemically defined conditions using Essential 8 (E8) medium and vitronectin (VN) as a coating substrate. To improve reproducibility, a defined number of hPSCs (10,000 cells/cm^2) was plated on VN-coated dishes in E8 medium supplemented with Chroman 1, Emricasan, Polyamines, and trans-ISRIB (CEPT) small-molecule cocktail for 24 h, which promotes optimal cell survival (Chen et al., 2021). On the following day, the cells were exposed to Astro-1 medium (Figure 1A; experimental procedures), formulated to modulate several cell signaling pathways with importance for RGC differentiation, including NOTCH and JAK/STAT (Deverman and Patterson, 2009). Daily Astro-1 medium changes resulted in efficient neuralization and formation of large numbers of neural rosettes over the course of 7 days (Figures 1B–1D). These cells were strongly immunoreactive for the RGC markers FABP7 (also known as brain lipid-binding protein [BLBP]), PAX6, and the proliferation marker KI-67 (Figures 1B and 1C). Two additional hPSC lines were successfully differentiated into rosette-forming RGCs expressing FABP7 and PAX6 (Figures S1A and S1B). We then compared the neural rosettes generated with our strategy with a widely used neural induction method known as dual SMAD inhibition (dSMADi) (Chambers et al., 2009). We performed unbiased high-content imaging of neuralized cultures (day 7) after performing immunocytochemistry for the tight junction marker ZO-1 to label the lumens of neural rosettes (Elkabetz et al., 2008; Figure 1D). Image analysis of regions of interest (ROIs) showed increased values in three independent cell lines indicating improved neural rosette structures with Astro-1 medium versus dSMADi (Figure 1E). Next, we performed RNA sequencing (RNA-seq) experiments to compare our novel neural induction strategy with dSMADi. Neural cells generated by Astro-1 versus dSMADi were different in their expression of RGC genes (Figure 1F). After normalization to gene expression in pluripotent cells, 44 genes were found to be differentially expressed, with Astro-1 inducing 37 genes and dSMADi inducing 7 genes. Of those 37 genes, 15 genes were reported to be enriched in brain-derived RGCs (Nowakowski et al., 2017): *BNIP3*, *HIST1HD*, *HMMR*, *KIF20A*, *TRIM24*, *ASPM*, *BIRC5*, *CACHD1*, *FAT1*, *HIST1H1B*,

Figure 1. Controlled RGC differentiation from hPSCs

(A) Schematic depicting RGC and astrocyte differentiation from hPSCs using chemically defined Astro-1, Astro-2, and Astro-3 media (see experimental procedures for details).

(B) Representative immunostaining of RGC cultures (day 7), showing neural rosettes expressing PAX6 and FABP7 derived from iPSCs (NCRM5). See Figure S1 for experimental replicates in hESCs (WA09) and iPSCs (LiPSC GR 1.1).

(C) Representative immunostaining of RGCs (day 7, NCRM5) and neural rosettes expressing the proliferation marker KI-67 and PAX6.

(D) High-content microscopy image analysis of RGC cultures (day 7, WA09), showing neural rosettes expressing ZO-1. ROI is defined as the regions of ZO-1 expression are depicted by a mask in yellow.

(E) Quantification of ROI in one hESC (WA09) and two iPSC lines (NCRM5 and LiPSC GR 1.1). The central area of a well (6 well plate) was imaged using 10× magnification and the Opera Phenix high-content imager (PerkinElmer). Data points in bar graphs represent analyzed images, and different colors of data points represent replicate wells; n $\geq$ 132 fields of view analyzed from a minimum of 2 replicate wells for each experimental condition. Three independent hPSC lines were tested.

(F) Heatmap showing differentially expressed RGC genes after neural induction with dSMADi and Astro-1. Samples obtained from three independent differentiation experiments are shown in the heatmap (LiPSC GR 1.1).

(G and H) In situ hybridization of the human fetal cortex at post-conceptual week 15, demonstrating expression of *FABP7* (G) and *PAX6* (H). Note the absence of *PAX6* from the cortical plate and the lateral and medial ganglionic eminence (LGE and MGE, respectively). Source of images: Allen Brain Atlas.

(I) Western blot analysis of OCT4, PAX6, FABP7, and SOX9. See the difference in FABP7 and SOX9 between cultures differentiated with Astro-1 versus dSMADi. RGCs (Astro-1) and NPCs (dSMADi) were derived from LiPSC GR 1.1.

(J) *BIRC5* expression in RGCs as detected by *in situ* hybridization (RNA-scope) after differentiation of iPSCs (LiPSC GR 1.1) in Astro-1 medium versus dSMADi (day 7).

(K) Quantification of *BIRC5* mRNA transcripts normalized to DAPI$^+$ nuclei; n = 4 replicate wells.

(L) Representative images of cells labeled for ASPM and PAX6 on day 7 (LiPSC GR 1.1).

(M) Quantification of the mitotic spindle protein ASPM normalized to PAX6$^+$ cells after differentiation with Astro-1 versus dSMADi; n = 4 replicate wells (LiPSC GR 1.1).

All data are presented as mean ± SD. Scale bars, 100 μm.

HIST1H1C, *HIST1H1E*, *HIST2H2BE*, *LDHA*, and *NUSAP1*. In contrast, one RGC gene, *PSAP*, was induced by dSMADi. The atypical cadherin FAT1 controls RGC proliferation, and its loss leads to abnormal radial glia morphology and neural tube defects (Badouel et al., 2015). We found that FAT1 was strongly expressed by neural rosettes (Figure S1E and S1F). Moreover, the RGC marker FABP7 was expressed at higher levels in cells generated with Astro-1 versus dSMADi, whereas PAX6 was expressed at comparable levels, and OCT4 was undetectable in either condition on day 7 (Figure 1I). Notably, *FABP7* is widely expressed by RGCs across the developing brain, whereas *PAX6* is restricted to the more anterior regions, such as the dorsal forebrain and diencephalon (Figures 1G and 1H; source: Allen Brain Atlas). SOX9 is an important regulator of glial cell fate (Kang et al., 2012) and was also expressed at higher levels in cells treated with Astro-1 (Figure 1I). Other genes of interest are *BIRC5* (*SURVIVIN*) and *ASPM*, which control RGC symmetric cell division and maintenance *in vivo* (Fish et al., 2006; Jiang et al., 2005). Quantitative *in situ* hybridization (RNA-scope) showed that *BIRC5* transcripts were higher in Astro-1 versus dSMADi (Figures 1J and 1K). Similarly, a trend increase was noted for the mitotic spindle assembly protein ASPM in cultures treated with Astro-1 (Figures 1L and 1M). Next, we tested whether these RGCs could be patterned by using developmental cues. Indeed, the telencephalic marker FOXG1 was reduced when CHIR99021 (a WNT activator) was added to Astro-1 medium (Figure S1M), whereas expression of the hindbrain marker HOXA2 was induced (Figure S1O). Adding FGF8 and CHIR99021 to Astro-1 medium reduced FOXG1 expression (Figure S1M) without HOXA2 induction (Figure S1O), while OTX2 expression was detected (Figure S1N), suggesting a midbrain-like identity. These findings were confirmed by using 3 different hPSC lines. Importantly, this experiment also validated FOXG1 protein expression in RGCs (Figure S1M). Collectively, we conclude that Astro-1 medium differentiates hPSCs directly into early RGCs with improved cell type identity compared with dSMADi.

The activated epidermal growth factor (EGF) pathway contributes to RGC-to-astrocyte differentiation at the expense of neurogenesis

To culture proliferative RGCs in Astro-1 medium, it was important to passage cells at defined time points to avoid overcrowded cultures that can result in cell contact inhibition and compromise directed differentiation. Cells were passaged on days 7, 11, and 14 and plated at 20,000, 30,000, and 40,000 cell/cm^2, respectively, to compensate for the decreased proliferation rate over time. Cells were passaged in the presence of the CEPT cocktail (Chen et al., 2021). By day 15, all cells adopted a flat morphology, and approximately 50% of the cells expressed the glial marker S100B (Figures S1G and S1H). At this stage, we removed LDN-193189 and platelet-derived growth factor (PDGF)-AA and added a lipid supplement to provide a more enriched medium (Astro-2 medium), which was necessary when culturing cells in the absence of animal serum (Figure 1A; experimental procedures). Astro-2 medium supplemented with lipids enabled glial differentiation completely under serum-free conditions (experimental procedures). S100B$^+$ cells were less proliferative, and passaging was carried out twice (days 18 and 23). We compared our approach with previous strategies that used either the mitogens EGF and FGF2 or serum-based differentiation (FBS + LIF) to promote the gliogenic switch (Krencik et al., 2011; Tchieu et al., 2019). When RGCs were treated with Astro-1 for 1 week followed by another week of Astro-2 treatment, the critical gliogenic transcription factor nuclear factor Ia (NFIA) (Deneen et al., 2006; Tchieu et al., 2019) was strongly induced. In contrast, NFIA was completely absent when RGCs were treated with EGF/FGF2 or 2% FBS and LIF (Figures 2A–2C). Strikingly, the neuronal marker beta-tubulin 3 (TUBB3) was not induced in cultures differentiated with the Astro-1/Astro-2 combination, whereas the two other tested conditions strongly induced TUBB3 (Figure 2D). We also noted that the glia marker CD133 (prominin-1) was expressed at higher levels after Astro-1/Astro-2 treatment (Figure 2E). To further examine whether the Astro-1/Astro-2 combination is more potent at inducing NFIA, we tested different treatment combinations over the course of 21 days (Figure S2A). Again, by using 3 different hPSC lines, we observed that the strongest average NFIA protein induction was due to Astro-1/Astro-2 treatment (Figures S2B and S2D). Interestingly, dSMADi followed by cell expansion with EGF/FGF2 resulted in the strongest TUBB3 induction (Figures S2B and S2D). Collectively, these experiments not only underscored the importance of Astro-1/Astro-2 media for glia-exclusive differentiation but also demonstrated that RGCs were capable of neuronal fate choice. Next, because Astro-1/Astro-2 media do not include EGF receptor ligands (Figure 1A; experimental procedures) but EGF receptor (EGFR) signaling has been implicated in gliogenesis (Burrows et al., 1997), we further investigated a role of the EGF pathway. To this end, we compared EGFR expression and downstream signaling under three different conditions using three different hPSC lines. Treatment groups included (1) dSMADi followed by EGF/FGF2 treatment, (2) Astro-1/Astro-2, and (3) Astro-1/Astro-2 combined with EGF/FGF2 treatment. Strikingly, strong expression of EGFR was found in all three cell lines after Astro-1/Astro-2 treatment but not when other conditions were used (Figure 2F). This correlated with strong phosphorylation of AKT (Figures 2F and 2G), suggesting that Astro-1/Astro-2 treatment resulted in activated EGF pathway signaling.

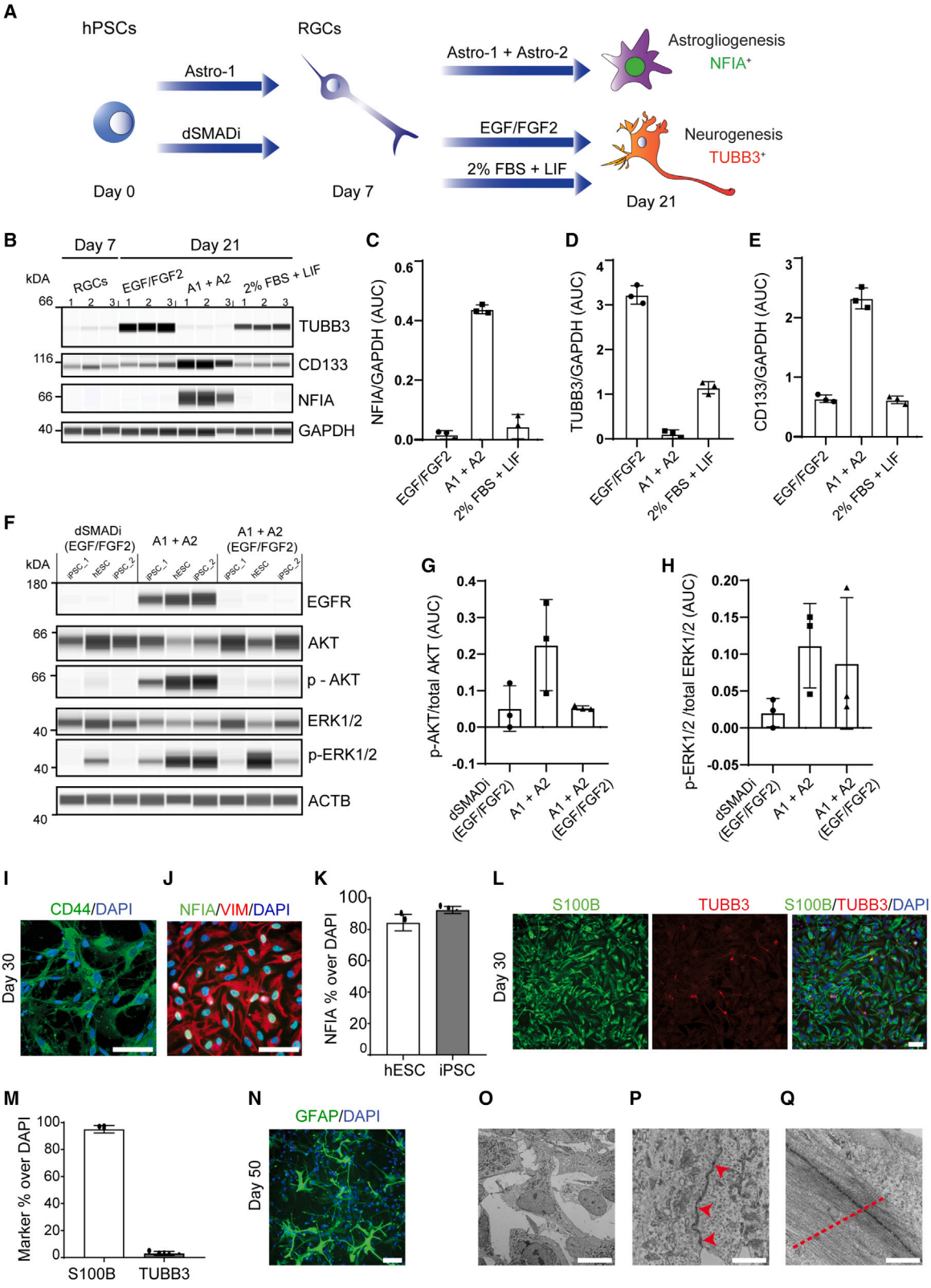

(legend on next page)

We also observed that Astro-1/Astro-2 increased phosphorylation of ERK1/2, although variability was found across the different cell lines and treatment conditions (Figure 2H). Unexpectedly, exogenous administration of EGF/FGF2 suppressed EGFR expression and AKT phosphorylation. This finding warrants future investigation, but the experiments described above suggested an important role of EGFR signaling in human gliogenesis even in the absence of recombinant EGF. Next, when culturing cells in Astro-2 until day 30 (Figure 1A), virtually all cells expressed CD44, and more than 85% of total cells expressed NFIA (Figures 2I–2K). At this stage, immunostaining for glial fibrillary acidic protein (GFAP) showed a diffuse signal (Figure S1I), but further maturation in Astro-3 medium (Figure 1A; experimental procedures) produced typical morphologies and GFAP expression (Figures S1D and S1J). Again, this observation was confirmed in several hPSC lines (Figure S1D). To demonstrate the purity of our astrocyte cultures, we performed immunostaining and quantitative analysis, revealing that more than 90% of total cells expressed the glial marker S100B by day 30, with only sporadic occurrence of neurons (3% of total cells) (Figures 2L and 2M). Electron microscopy analysis (days 30 and 50) did not detect neurons, and the derived astrocytes were comparable with control astrocytes (Figure S1J), displaying star-shaped morphologies (Figure 2O) and abundant cytoplasmic intermediate filaments (Figures 2Q and S1L). Astrocytes were rich in organelles such as the endoplasmic reticulum (ER) and Golgi apparatus, indicating secretory activity (Figures S1J and S1K). Well-developed cell junctions were also frequently observed (Figures 2P and S1L).

To test whether RGCs could produce other neural cell lineages, we generated brain organoids (Figure S1P) following a published protocol (Marton et al., 2019). RGCs formed spheroids (Figure S1Q) and developed neural tube-like structures (Figures S1P and S1R). In different experiments, we asked whether RGCs can be patterned into oligodendrocyte precursors (Lager et al., 2018). When SAG21K, an activator of sonic hedgehog (SHH) signaling, and retinoic acid were added to Astro-1 medium, OLIG2$^+$ cells were generated using two different hPSC lines (Figure S1S). Together, hPSC-derived RGCs displayed appropriate developmental plasticity and produced various neural lineages under different conditions.

Transcriptomic changes confirm RGC and fetal-like astrocyte identity

Time-course RNA-seq experiments were performed to characterize human gliogenesis under defined *in vitro* conditions. Principal-component analysis (PCA) showed distinct clustering of samples across six different time points (Figure 3A). Unbiased comparison of the top 100 differentially upregulated genes using the ARCHS4 tissue database,

Figure 2. Efficient glial differentiation of RGCs with Astro-1 and Astro-2

(A) Experimental design to compare different neural precursors and media.

(B) Western blot analysis of RGCs and neural precursors (day 7) and after treatment for 2 weeks with EGF/FGF2 (25 ng/mL each), Astro-1 and Astro-2 (A1+ A2), or 2% FBS + LIF (10 ng/mL) (NCRM5).

(C–E) Quantification of western blots normalized to GAPDH and performed in triplicates for NFIA (C), TUBB3 (D), and CD133 (E) expression after different treatments. Note the strong expression of NFIA and CD133 after culture in Astro-1/Astro-2 medium and the absence of TUBB3. Three independent experiments were performed (NCRM5).

(F) Western blot analysis of day 21 cultures treated with (1) dSMADi (days 0–7) and EGF/FGF2 (days 7–21), (2) Astro-1/Astro-2, or (3) Astro-1/Astro-2 supplemented with EGF/FGF2 (25 ng/mL each). Replicates represent 3 different hPSC lines (WA09, LiPSC GR 1.1, and NCRM5).

(G and H) Quantification of phosphorylated proteins normalized to total protein for p-AKT (Ser473) expression and p-ERK1/2 (Thr202/Tyr204). Shown are replicates of 3 different hPSC lines (WA09, LiPSC GR 1.1, and NCRM5).

(I and J) Astrocytes expressing CD44, NFIA, and VIMENTIN on day 30 (NCRM5). See Figure S1 for experimental replicates with hESCs (WA09) and iPSCs (LiPSC GR 1.1).

(K) Quantification of NFIA$^+$ nuclei normalized to total number of nuclei (day 30). n = 4 replicate wells for 2 independent cell lines (WA09 and LiPSC GR 1.1).

(L) Immunostaining of cultures (day 30), showing S100B and TUBB3 expression (LiPSC GR 1.1).

(M) Quantification of S100B- and TUBB3-immunoreactive cells normalized to DAPI$^+$ nuclei. n = 4 replicate wells for 2 independent cell lines (WA09 and LiPSC GR 1.1).

(N) Immunostaining showing astrocytes with stellate morphology and GFAP expression (day 50, NCRM5). See Figure S1 for experimental replicates (WA09 and LiPSC GR 1.1).

(O) Electron microscopy confirms typical astrocyte morphologies (day 50).

(P) Depiction of *zonula adherens* at the ultrastructural level (red arrowheads).

(Q) Presence of abundant intermediate filaments (red dashed line). For ultrastructural analysis, 3 independent samples were included (day 30, day 50 iPSC-astrocytes [NCRM5], and controls [iCell Astrocytes Fujifilm CDI]). See Figure S1 for more details.

All data presented as mean ± SD. Scale bars, 100 μm (I, J, L, and N), 2 μm (O), and 500 nm (P and Q).

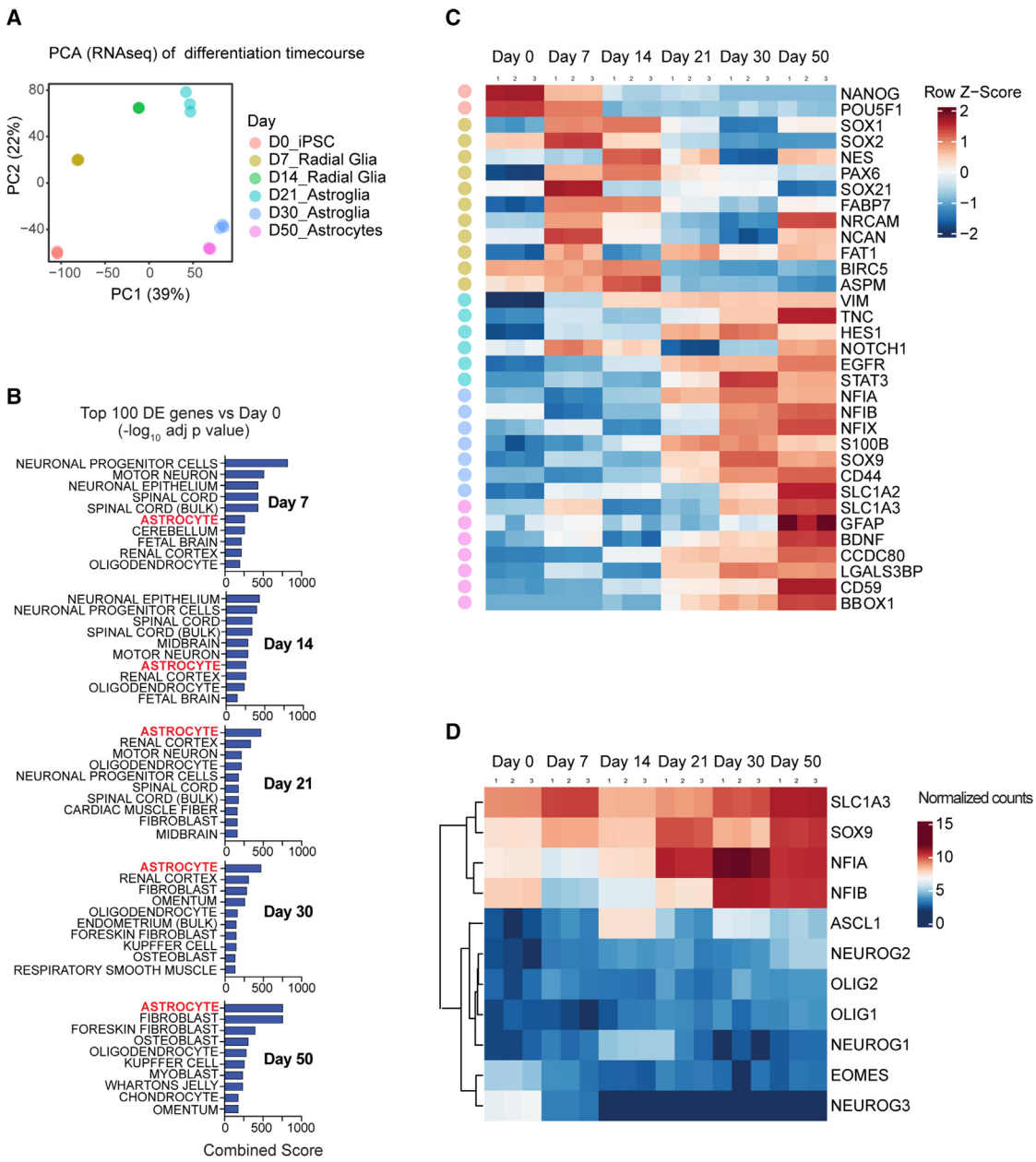

Figure 3. Transcriptomic analysis of hPSCs differentiating into RGCs and astrocytes

(A) PCA of time-course RNA-seq experiments of iPSCs (day 0) and differentiating cells (days 7, 14, 21, 30, and 50) (NCRM5).

(B) Heatmap depicting cell-type-specific genes at different time points, including pluripotent cells (day 0), RGCs (days 7 and 14), astroglia (days 21 and 30), and astrocytes (day 50).

(C) Gene enrichment analysis (ARCHS4 and Enrichr) based on the top 100 differentially upregulated genes (p_{adj}) versus hPSCs (day 0) reveals "astrocytes" as the top hit starting on day 21.

(D) Heatmap with average linkage dendrogram showing induction of astrogliogenic transcription factors (e.g., *SOX9*, *NFIA*, and *NFIB*) and absence of genes representative of neurogenesis (*NEUROG 1/2/3* and *EOMES*) and oligodendrogenesis (*OLIG1/2*).

n = 3 independent astrocyte differentiation experiments (NCRM5).

which contains 84,863 transcriptomes of diverse human samples, and the gene enrichment platform Enrichr (Lachmann et al., 2018), underscored stepwise differentiation, resulting in "astrocyte" as the top category by days 21, 30, and 50 (Figure 3B). Heatmap analysis showed cell type- and stage-specific gene expression and the transcriptional

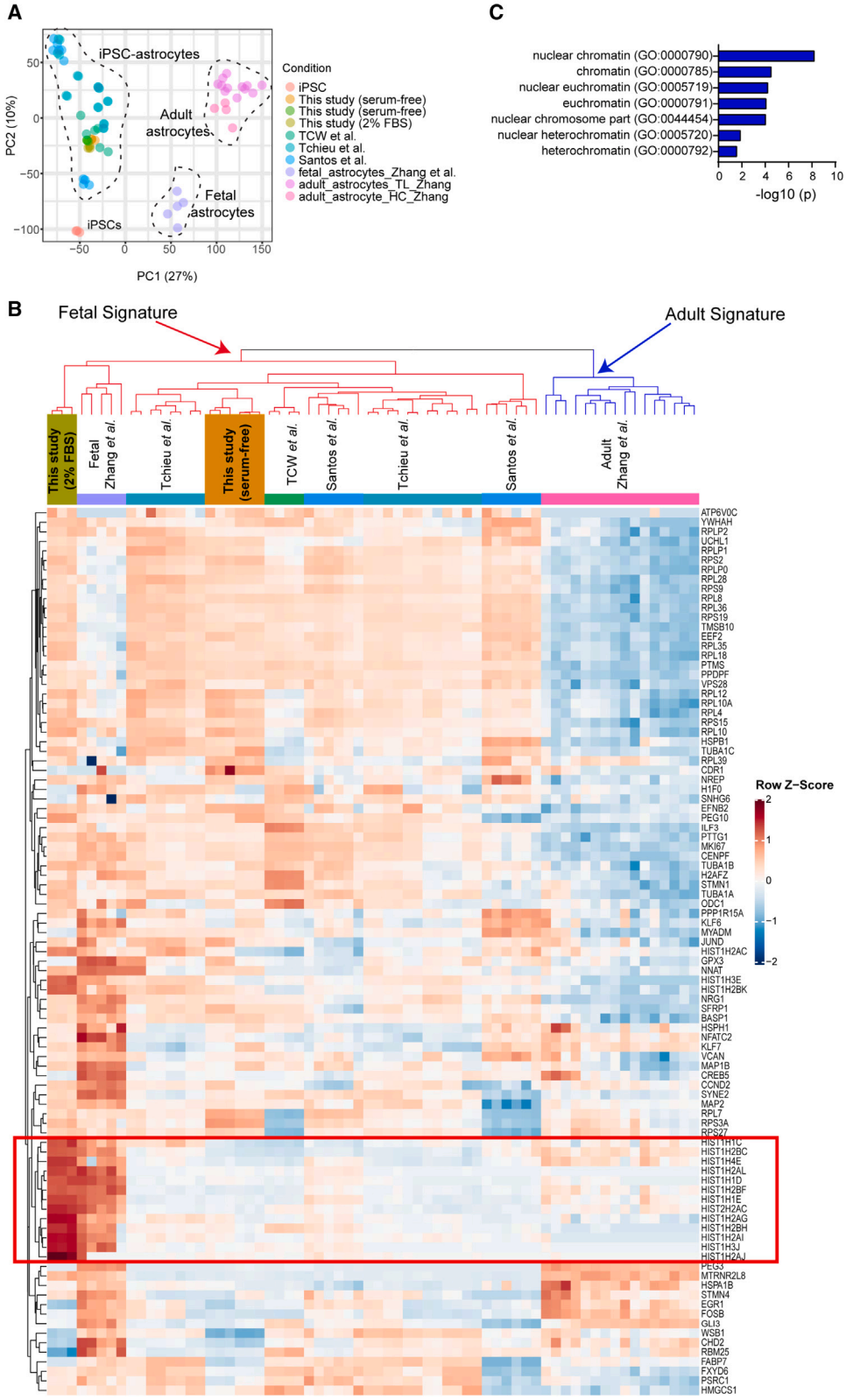

(legend on next page)

changes, consistent with stepwise and controlled gliogenesis (Figure 3C). Accordingly, the pluripotency-associated genes *OCT4* and *NANOG* were downregulated by day 7, whereas *NOTCH1*, *FABP7*, *PAX6, NESTIN* (*NES*), *NRCAM*, and *NCAN* were strongly induced in RGCs (Figure 3C), as also confirmed by immunocytochemistry and western blot analysis (Figures 1B, 1I, and S1). By days 14 and 21, additional radial glia markers (*VIMENTIN* [*VIM*] and *TENASCIN C* [*TNC*]) were expressed by RGCs. By day 30, cells expressed canonical astrocyte markers (e.g., *NFIA*, *NFIB*, *S100B*, and *CD44*) and glutamate transporters (*SLC1A2/EAAT2* and *SLC1A3/GLAST*). Throughout differentiation (days 0–50), we did not detect induction of pro-neuronal transcription factors (*NEUROGENIN 1*, *NEUROGENIN 2*, *NEUROGENIN 3*, and *EOMES)*. In contrast, the gliogenic transcription factors *SOX9*, *NFIA*, and *NFIB* (Canals et al., 2018; Li et al., 2018b) were strongly expressed from day 14 onward (Figure 3D). We also confirmed the absence of oligodendrocyte precursor markers (*OLIG1* and *OLIG2*) throughout the astrocyte differentiation process (Figure 3D). Together, these findings document that RGCs can be directly differentiated into astrocytes without going through a neurogenic phase or artificially inducing the gliogenic switch by forced expression of *NFIA* in expanded NSCs (Tchieu et al., 2019).

Next, we compared the transcriptomic profiles of astrocytes generated with the present method with previously published reports differentiating hPSCs (Santos et al., 2017; Tchieu et al., 2019; Tcw et al., 2017) and primary astrocytes from fetal and adult human brains (Zhang et al., 2016) (Figure 4A). After batch correction based on expression of 50 "housekeeping" genes, we performed unsupervised hierarchical clustering, focusing on the genes expressed in human fetal astrocytes (Zhang et al., 2016). Our serum-free astrocyte cultures and hPSC-astrocytes of other studies clustered together with samples of primary fetal astrocytes and away from the primary adult astrocytes (Figure 4B). In addition, we treated our astrocyte cultures with 2% FBS, which has been used in other studies (Santos et al., 2017; Tchieu et al., 2019; Tcw et al., 2017). FBS led to a strong induction of genes encoding histone proteins (Figures 4B and 4C), a signature that was also found in primary human fetal astrocytes (Zhang et al., 2016) but not in hPSC-astrocytes reported previously (Santos et al., 2017; Tchieu et al., 2019; Tcw et al., 2017). Next, we addressed whether hPSC-astrocytes showed a distinct regional identity. To perform this analysis in an unbiased fashion, we determined gene sets by focusing on the top 10 genes with the strongest expression across 8 different brain regions during fetal human brain development (CS22) (Eze et al., 2021). Heatmap clustering analysis demonstrated strong expression of cortical markers such as *LHX2*, *TCF4*, *FEZF2*, and *FGFR3* in the primary adult cortical astrocytes (Figure S2E). Fetal brain astrocytes expressed regional markers from across different brain regions, such as *STMN2* (hindbrain), *MEG3* (hypothalamus), and *BCL11B* (ganglionic eminence), which were not observed in the adult cortical astrocytes (Figure S2E). Despite molecular similarity to fetal astrocytes, hPSC-astrocytes presented an even more diverse expression pattern of regional markers, suggesting an early pre-specification stage (Figure S2E).

Functional characterization of human astrocytes

When co-culturing hPSC-astrocytes and controls with glutamatergic cortical neurons for 8 days, multi-electrode array (MEA) experiments showed enhanced neuronal activity compared with neuron-only cultures. By day 8, neurons co-cultured with astrocytes displayed robust electrical activity (Figure S3A), as indicated by a larger number of spikes (Figure S3B), higher average number of active electrodes (Figure S3C), and robustness of spike intervals across wells (Figure S3D) compared with neuron-only cultures. Next, when astrocytes were co-cultured with glutamatergic neurons for 21 days, the synaptic vesicle protein synaptophysin (SYP) was expressed at higher levels. Similarly, co-culturing resulted in stronger expression of vesicular glutamate transporter 1 (VGlut1) and S100B, which suggests a reciprocal cell maturation effect of both cell types compared with monoculture conditions (Figure S3E). To measure neuronal survival and neurite outgrowth, hPSC-astrocytes were co-cultured with i3 neurons (Fernandopulle et al., 2018), stably expressing green fluorescent protein (GFP) in the nucleus and red fluorescent protein (RFP) in the cytoplasm. To quantify neurite length, continuous live-cell imaging was performed (IncuCyte). i3 neurons co-cultured with astrocytes developed neurites with

Figure 4. Comparative transcriptomic analysis of hPSC-derived astrocytes

(A) PCA plot of iPSCs and astrocytes generated in the present study (serum free and 2% FBS) and comparison to previous studies after performing batch correction.

(B) Hierarchical clustering based on the top 100 genes expressed by primary human fetal astrocytes according to Zhang et al. (2016). Note that genes regulating histone proteins are strongly induced in iPSC-derived astrocytes (day 30) after adding 2% FBS to Astro-2 medium, making them more similar to fetal brain-derived astrocytes (red boxed area).

(C) Gene enrichment analysis of the prominent histone gene cluster that was induced by 2% FBS (red boxed area in B).

n = 3 independent differentiation experiments (NCRM5) for each of the sample groups included in SRA batch correction from this study (depicted in green and orange in A and B).

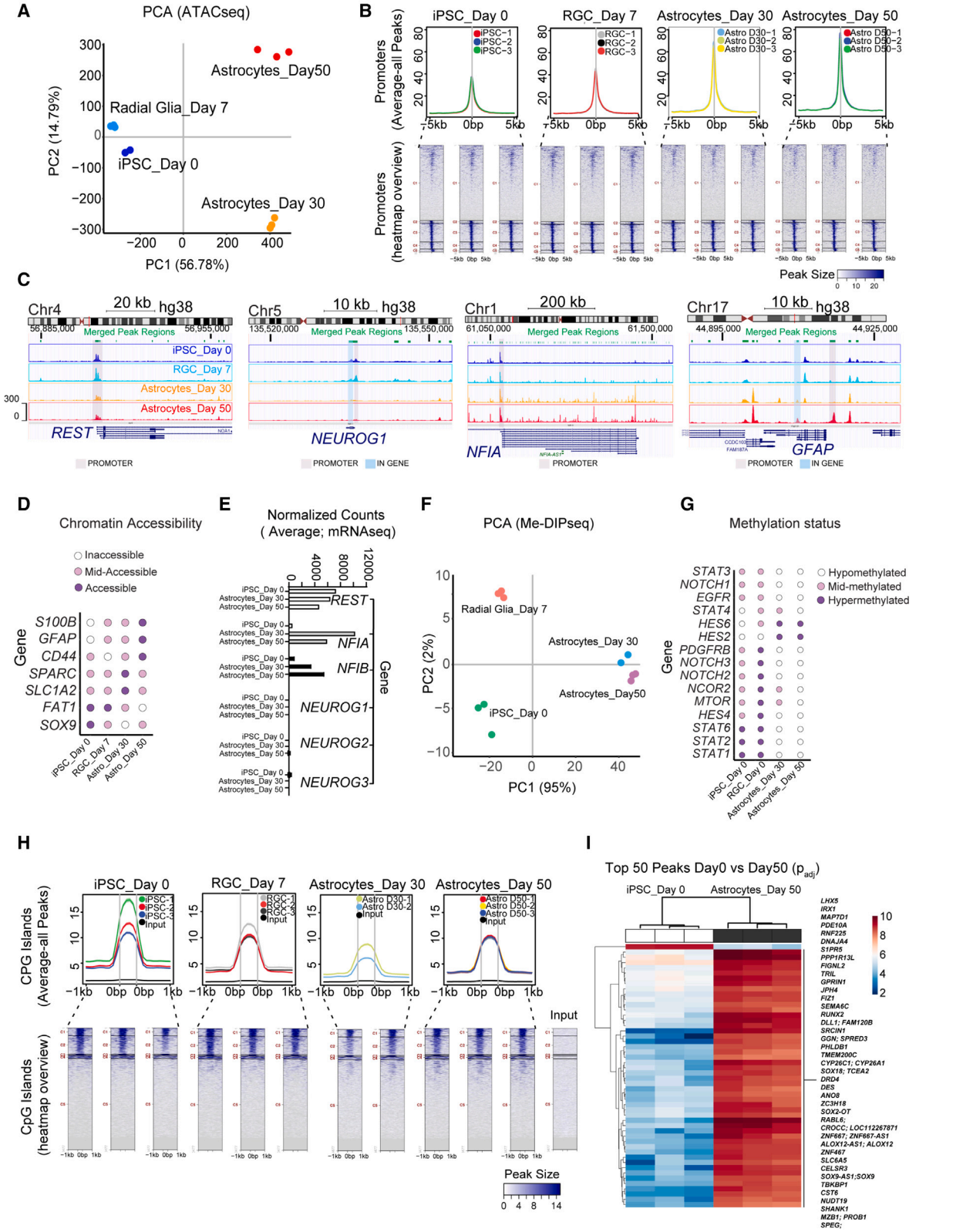

(legend on next page)

increased length (Figures S3F and S3G). Periodic acid-Schiff (PAS) staining confirmed intracellular glycogen accumulation (Figure S3H). Similar to their *in vivo* properties, hPSC-astrocytes were able to remove extracellular glutamate (Figure S3I) and also secreted human complement factor C3 in response to an inflammatory cocktail (interleukin-1b [IL-1b], tumor necrosis factor alpha [TNF-α], and C1Q) (Figure S3J). The use of a fluorescence imaging plate reader (FLIPR) revealed that hPSC-astrocytes (day 30) can elicit calcium transients when stimulated with KCl, ATP, and L-glutamate (Figure S3K). As a normal physiological response, astrocytes can release intracellular calcium through IP3 receptor 2 (IP3R2), expressed on the ER (Sherwood et al., 2021). We tested ATP-induced calcium transients after selective inhibition of IP3R and observed a dose-dependent reduction in the calcium response (Figures S3L and S3M). Astrocyte cultures also displayed slow spontaneous calcium transients spreading across larger cell populations (Video S1), which was comparable with control astrocytes (Video S2).

Epigenetic regulation of human astrogliogenesis

We mapped epigenetic changes by performing genome-wide analyses of chromatin accessibility using the assay for transposase-accessible chromatin with sequencing (ATAC-seq) and DNA methylation by employing methylated DNA imunoprecipitation sequencing (MeDIP-seq) at different time points (days 0, 7, 30, and 50). Distinct chromatin signatures were observed over the time course (Figure 5A). Global promoter accessibility, defined as the average ATAC-seq signal in peaks 5 kb upstream or downstream of the transcription start site (TSS), increased as iPSCs differentiated into RGCs and astrocytes (Figure 5B). The overall number of peaks detected in promoter regions was reduced (Figure 5B). We studied the gene loci of *REST* (RE1 silencing transcription factor), a master negative regulator of neurogenesis involved in transcriptional repression of neuronal genes in non-neuronal cells (Ballas et al., 2005; Lunyak and Rosenfeld, 2005; Shi et al., 2004). The promoter region of *REST* remained accessible, and *REST* transcripts, as also confirmed by RNA-seq, were expressed throughout the glial-specific differentiation trajectory (Figures 5C and 5E). In contrast, the promoter and gene body of pro-neuronal transcription factor *NEUROGENIN1* (*NEUROG1*), known to induce neurogenesis and inhibit gliogenesis (Sun et al., 2001), was inaccessible on days 30 and 50 (Figures 5C and 5E). The *NFIA* promoter was accessible throughout all time points, whereas the *NFIA* gene body was inaccessible in iPSCs (day 0) and RGCs (day 7) and then became largely accessible in astrocytes (days 30 and 50) (Figure 5C). Finally, open chromatin at the *GFAP* promoter was observed only in astrocytes on day 50 (Figure 5C), consistent with the onset of mRNA and protein expression (Figures 2N, 3C, and S1D). Focusing on a set of genes reported previously (Zhang et al., 2016), we identified two clusters (31 and 79 genes) with highly accessible regions (Figure S4A). Gene enrichment analysis revealed that the smaller cluster with the 31 genes annotated processes such as "cell migration" and "cell motility" (Figures S4B–S4E). The larger cluster of 79 genes indicated categories such as "cell cycle and "proliferation" (Figures S4D and S4E). Analysis of open chromatin regions showed highest chromatin accessibility for *SOX9* and *FAT1* on days 0 and 7, while *SLC1A2* and *SPARC* showed highest accessibility on day 30, and *S100B* and *GFAP* were most accessible on day 50 (Figure 5D).

Figure 5. Genome-wide chromatin accessibility (ATAC-seq) and DNA methylation (MeDIP-seq)

(A) PCA plot of differentiating iPSCs (NCRM5) harvested at different time points (days 0, 7, 30, and 50) to study chromatin accessibility (ATAC-seq).

(B) Top row: average plots for all peaks across target promoter regions defined as TSS ± 5 kb. Bottom row: heatmap representation of all peaks within promoter regions.

(C) UCSC Genome Browser plots showing merged peak regions in *REST*, *NEUROG1*, *NFIA*, and *GFAP* gene loci. Note that the *REST* gene promoter remains accessible throughout differentiation. See the global closure of the *NEUROG1* region and the global opening of *NFIA* on days 30 and 50. The *GFAP* promoter region is open on day 50.

(D) Dot plot of chromatin accessibility, representing peaks of highest variance in genes expressed by RGCs and astrocytes.

(E) Normalized counts (RNA-seq) of gliogenic and neurogenic genes at different time points. Note that *REST* remains expressed throughout the entire differentiation process.

(F) PCA plot of samples used to study DNA methylation (MeDIP-seq).

(G) Dot plot of DNA methylation, showing peaks with highest variance for genes associated with NOTCH and JAK/STAT signaling: mTOR, NCOR2, and others.

(H) Top row: average plots for all peaks across target promoter regions defined as CpG island ± 1 kb. Bottom row: heatmap representation of all peaks within CpG island regions.

(I) Heatmap of top 50 differentially methylated peaks in iPSCs (day 0) versus astrocytes (day 50). Note that most peaks represent hypermethylated regions within genes (49 of 50) in astrocytes. See Figure S5 for UCSC Genome Browser plots depicting representative gene loci from this heatmap.

n = 3 independent astrocyte differentiation experiments for all datasets presented (NCRM5).

Next, we studied DNA methylation changes over the course of cell differentiation (Figure 5F). Global CpG island hypermethylation, defined as the average MeDIP-seq signal in peaks 1 kb upstream or downstream of the CpG island region, was slightly reduced over the time course of RGC and astrocyte differentiation, while the overall number of peaks increased (Figure 5H). The correlation analysis of peaks (Pearson coefficient) across all samples showed more dramatic changes in chromatin accessibility compared with methylation (Figures S5A and S5B). Of the top 50 most differentially methylated regions between iPSCs and astrocytes, 49 were hypermethylated in astrocytes (Figure 5I). Among these hypermethylated genes were the pro-neuronal transcription factors *IRX1* and *LHX5* (Cohen et al., 2000; Li et al., 2021) and several genes involved in neuronal function (*SHANK1*, *GPRIN1*, and *JPH4*) (Hogea et al., 2021; Hung et al., 2008)(Figure 5I). Sphingosine-1-phosphate receptor 5 (*S1PR5*), a gene involved in oligodendrocyte development (Jaillard et al., 2005), and *PHLDB1*, a gene associated with glioma susceptibility (Baskin et al., 2015), were also hypermethylated in day 50 astrocytes (Figure 5I). Collectively, these analyses substantiated an astrocyte-specific chromatin and methylation landscape (Figures 5I and S5C–S5H).

Next, we asked whether these methylation changes may shed light on the cellular pathways that govern astrogliogenesis. Focusing on the PCA of peaks with the highest variance, we analyzed the promoter regions of JAK/STAT, NOTCH, PDGF, *mTOR*, and *NCOR2* (Figure 5G). Components of JAK/STAT signaling (*STAT1*, *STAT2*, *STAT3*, *STAT4*, and *EGFR*), NOTCH (*NOTCH1*, *NOTCH2*, *NOTCH3*, and *HES4*), and the tyrosine kinase receptor *PDGFRB* were hypermethylated at the RGC stage and then hypomethylated in astrocytes (Figure 5G). *HES6* is an atypical HES gene that inhibits *HES1*, which is required for activation of *NEUROGENIN* and *NEUROD* (Murai et al., 2011). *HES6* was hypermethylated in astrocytes (Figure 5I). Last, hypomethylation of *mTOR* and *NCOR2* genes on day 50, but not in immature CD44^{+} astrocytes (day 30) or RGCs (day 7) (Figure 5I), may indicate potential roles during cell maturation. Indeed, unbiased comparative analysis of the top differentially methylated regions revealed that *NCOR2* hypomethylation was the most significant hit (Figure S4F). *NCOR2* hypomethylation correlated with increased chromatin accessibility and mRNA expression on day 50. Other differentially hypomethylated genes with potential roles in astrocyte maturation were *SYNJ2* and *DLG5*, which was also confirmed by transcript expression (Figures S4F, S4I, and S4J).

Single-cell transcriptomics identifies new astrocyte markers

To characterize the molecular underpinnings of RGC-to-astrocyte transition, we performed single-cell RNA-seq (scRNA-seq) of astrocytes (day 50) and compared them with control astrocytes and glutamatergic neurons. We profiled the transcriptomes of 12,771 cells, and unbiased clustering identified 11 transcriptionally distinct cell clusters: 4 representing neurons and 7 representing astrocytes (Figure 6A). Most cells in the astrocyte clusters were characterized by expression of *NFIA*, *HOPX*, *S100B*, and *GFAP*, while only a few cells expressed *AQP4* and HEPACAM, which are thought to be markers of more mature astrocytes (Sloan et al., 2017; Zhang et al., 2016). Neurons showed strong expression of typical markers, including *MAPT*, *NSG2*, *STMN2*, *SYT1*, *ANK3*, and *NRXN1* (Figure 6B). Heatmap analysis (top 10 genes per cluster) revealed more consistent gene expression across neuronal clusters, whereas astrocyte clusters were more heterogeneous (Figures 6C and S6D–S6G). Next, we performed extensive data integration with single-cell transcriptome data of the developing human telencephalon (Nowakowski et al., 2017). During early development, fetal astrocytes share high transcriptomic similarity with RGCs (Figures S6A–S6C). Data integration revealed 3 distinct clusters: radial glia, astrocytes, and cortical neurons (Figure S6B). The uniform manifold approximation and projection (UMAP) plot revealed bidirectional propagation toward mature astrocytes because cells clustered close to human cortical radial glia of dorsal (Figure S6B, red arrow) and the ventral ganglionic eminence (Figure S6C, blue arrow). This suggests that the first emerging RGCs lack regionalization and do not directly default into a cortical signature, which is consistent with our specification analysis (Figure S2E). To characterize astrocyte differentiation, we performed slingshot analysis (Street et al., 2018) and identified three different trajectories mapping transition of RGCs (pseudotime starting point) into two branches representing astrocytes and one "teleporting" RGCs to excitatory neurons because transitional states were not detected because our differentiation method bypasses neurogenesis (Figures 6D and 6E). The pseudotime starting point was marked by strong *MKI67*, *ASPM*, and *NUSAP1* expression in clusters 5 and 8, indicating RGC and immature astrocyte identities (Figures 6A, 6C, and 6E). Progression of RGCs into astrocytes did not lead to complete *MKI67* downregulation, whereas differentiated neurons were devoid of MKI67, suggesting a postmitotic state (Figures 6F and S6D–S6F). To identify new markers capturing RGC-to-astrocyte differentiation, we correlated gene expression variation with each of the cell types in pseudotime by performing trajectory-based differential expression analysis (tradeSeq) (Van den Berge et al., 2020). Along both astrocyte trajectories (Figure 6G, trajectories 1 and 3, yellow and purple lines), we observed induction of *GFAP* expression, while the neuronal trajectory displayed *MAP2* expression (Figure 6G, trajectory 2, green line). We subcategorized genes differentially

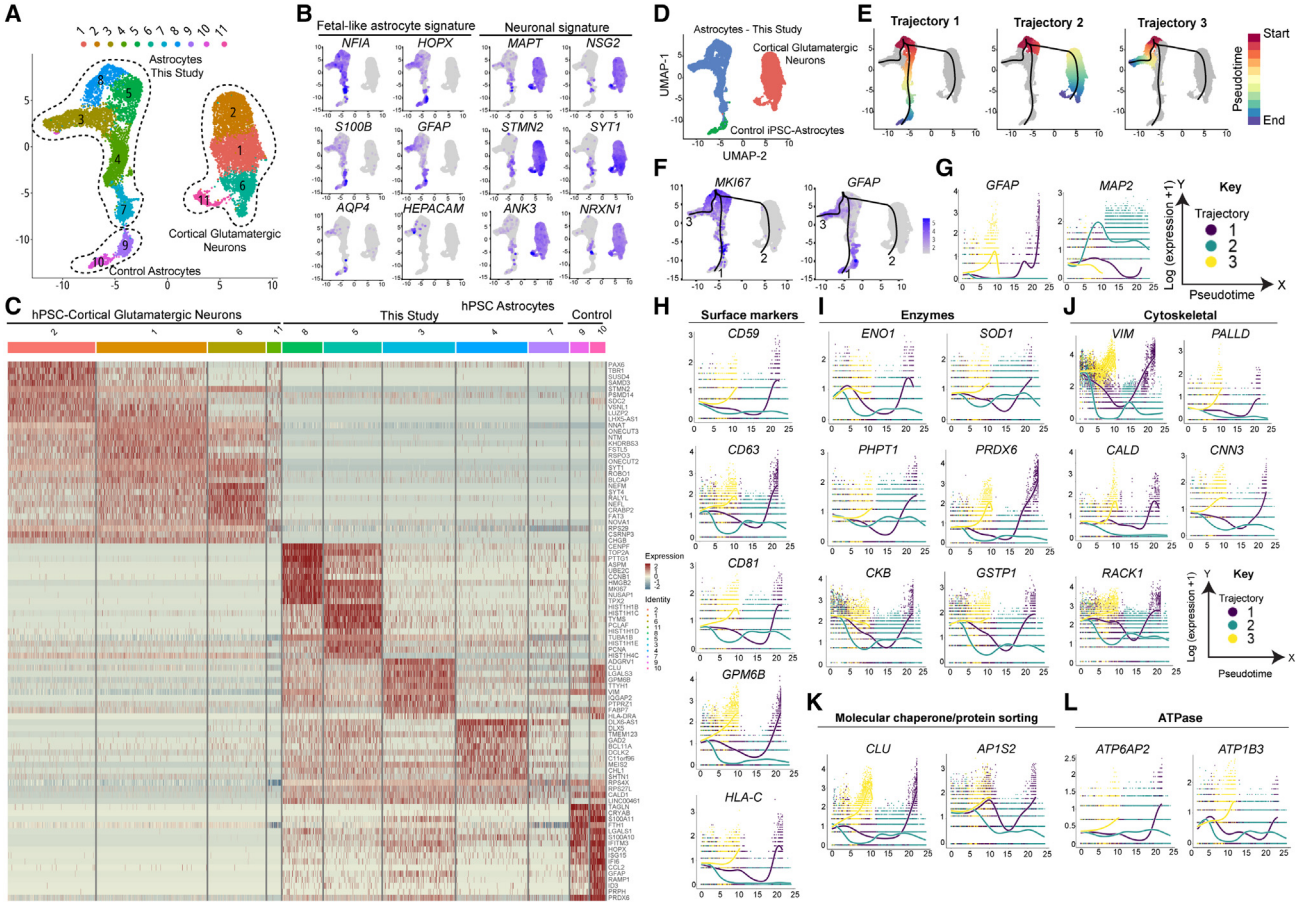

Figure 6. scRNA-seq analysis maps the fetal astrocyte signature and astrocyte maturation markers

(A) UMAP of 12,771 hPSC-derived neural cells showing 11 distinct cell clusters. Clusters are color coded, and dotted lines demarcate different cell types.

(B) Feature plots for genes expressed by fetal and adult astrocytes and neurons.

(C) Heatmap for the top 10 genes expressed across clusters. Rows correspond to genes and columns to cells/clusters. Blue/yellow, low gene expression; red, high expression. Note the clear difference between neuronal and astrocytic signatures.

(D) UMAP of 12,771 hPSC-derived neural cells color-coded by cell type. Blue, astrocytes generated in this study; green, control astrocytes (Fujifilm CDI); red, glutamatergic neurons (Fujifilm CDI).

(E) Slingshot analysis maps 3 different trajectories of cell progression. Red, pseudotime start point; blue, pseudotime endpoint.

(F) Feature plots for the *MKI67* and *GFAP* genes. Note that all pseudotime trajectories start within the clusters with high *MKI67* and low *GFAP* expression and progress to areas with high GFAP expression (1 and 3) or no GFAP expression (2, neurons).

(G) Gene expression dynamics relative to the previously identified trajectories performed using tradeSeq, showing *GFAP* induction along trajectories 1 and 3 (astrocytes) and *MAP2* induction along trajectory 2 (neurons).

(H–L) Genes representing surface markers, enzymes, cytoskeletal/scaffolding proteins, and others with differential induction in maturing astrocytes but not neurons. Data are from 12,771 single cells obtained from experiments using differentiated astrocytes from hESCs (WA09) and commercial products (iAstro and iGluta neurons, Fujifilm CDI). scRNA-seq data were analyzed in the Seurat R package.

upregulated in astrocytes into 5 different categories: surface markers, enzymes, cytoskeletal/scaffolding proteins, membrane-vesicle trafficking, and ATP transporters (Figures 6H–6L). Surface markers that were upregulated over the pseudotime and indicative of astrocyte maturation were *CD59*, *CD63*, *CD81*, *GPM6B*, and *HLA-C* (Figure 6H). Astrocytes also showed specific upregulation of enzymes involved in glucose metabolism (*ENO1*), oxidative metabolism (*SOD1* and *PRDX6*), glutathione biosynthesis (*GSTP1*), energy metabolism (*CKB*), and protein dephosphorylation (*PHPT1*) (Figure 6I). *VIM*, *GFAP*, and *S100B* are well-established astrocyte markers, and our analysis identified *PALLADIN* (*PALLD*) and *CALDESMON* (*CALD1*) as astrocyte enriched (Figure 6J). *CNN3* is a member of

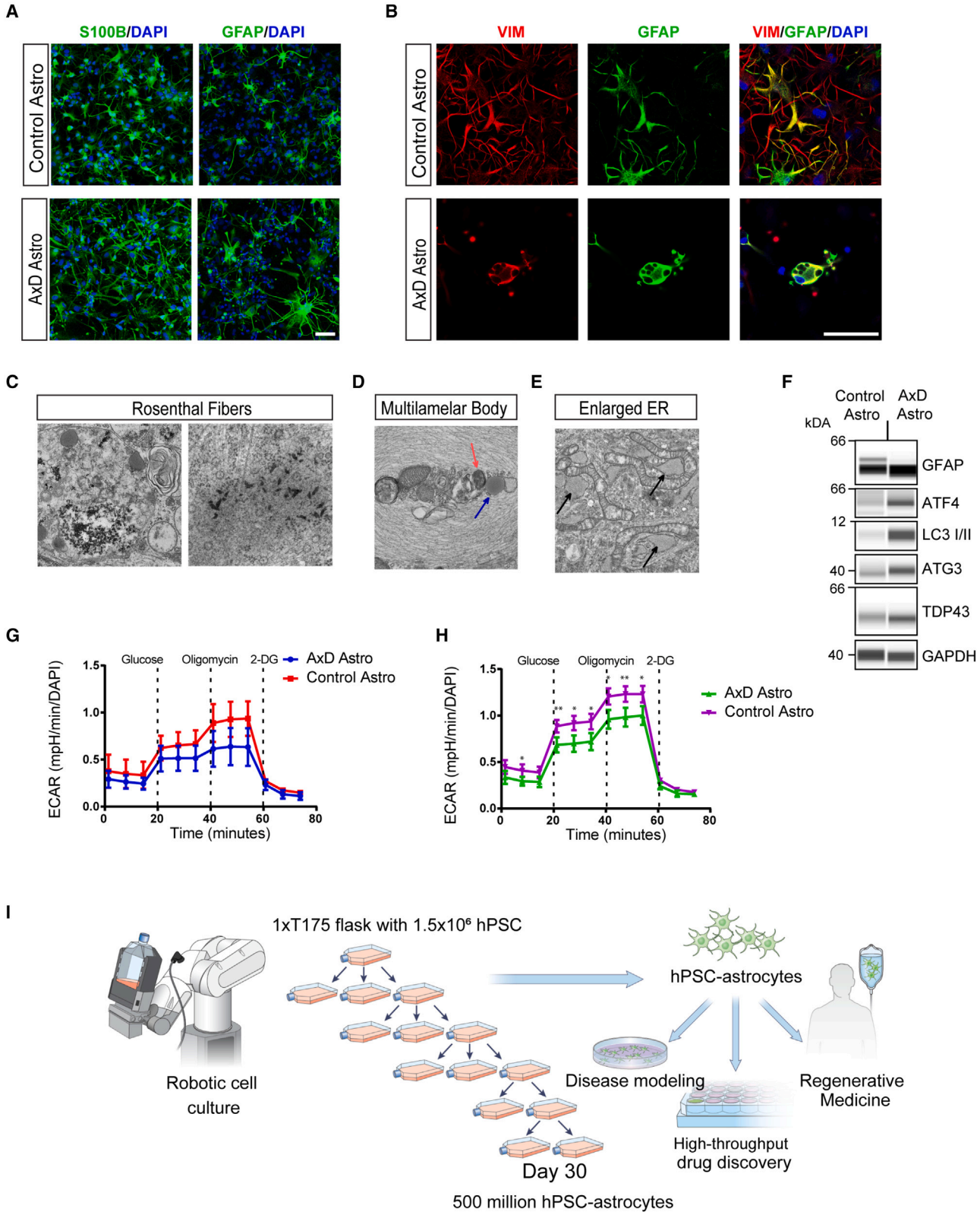

(legend on next page)

the calponin family of actin regulators, highly expressed in the mammalian brain, and involved in regulating the plasticity of dendritic spines (Junghans and Herzog, 2018). The receptor for activated C kinase (*RACK1*) is important for maintenance of neural progenitors (Zhu et al., 2021). *CNN3* and *RACK1* were strongly upregulated during astrocyte differentiation (Figure 6J). Similarly, the molecular chaperone *CLUSTERIN* (*CLU*) and clathrin-associated adaptor protein complex 1 (AP1S2) (Figure 6K) and specific ATPases (*ATP6A2* and *ATP1B3)* were strongly upregulated during astrocyte differentiation (Figure 6L). Together, these results uncover a set of novel markers that capture the directed differentiation of RGCs into astrocytes. Many of these genes are associated with neurodegenerative diseases (e.g., *SOD1*, *CLU*, *AP1S2*, and *ATP1B3*) and may serve as biomarkers and elucidate pathology.

Translational utility of hPSC-astrocytes

Next, we established a cellular model for Alexander disease (AxD) using an iPSC line from a patient with a mutation in codon 239 of the GFAP gene (729C > T) resulting in arg239-to-cys mutation *ARG239CYS* (R239C) (Brenner et al., 2001). Clinically, the patient presented with macrocephaly, and MRI scans showed white matter defects and ventricular cysts. The patient experienced first seizures at the age of 3.5 years and died at 6 years of age, with the diagnosis confirmed by autopsy. Using this iPSC line, we generated astrocytes expressing S100B and GFAP (day 50) and compared them with astrocytes from a non-isogenic control line (Figure 7A). Confocal microscopy showed aberrant morphology of AxD astrocytes with prominent GFAP$^+$ aggregates (Figures 7B and S7H), consistent with previous reports (Jones et al., 2018; Li et al., 2018a). Ultrastructural analysis revealed electron-dense material in the cytoplasm of AxD astrocytes, representing pathognomonic protein aggregates, the so-called Rosenthal fibers (Figure 7C). Other pathological changes included multi-lamellar body formation (Figure 7D) and an enlarged ER (Figure 7E). In contrast, these pathological phenotypes were not observed in healthy control astrocytes (Figures S1J–S1L). Furthermore, AxD astrocytes displayed an abnormal unfolded protein response (UPR), as indicated by ATF4/ATG3 protein upregulation. Elevated expression levels of the autophagy marker LC3I/II, GFAP, and total TDP-43, which is associated with several neurodegenerative diseases, suggested the presence of additional pathophysiological mechanisms in AxD astrocytes (Figure 7F). Metabolic profiling (Searhorse XF Analyzer) revealed impairment in glycolysis and glycolytic capacity in AxD astrocytes (Figures 7G and 7H).

To demonstrate that human astrocytes can be grafted, neonatal and adult mice received iPSC-derived astrocytes via unilateral injections, either intraventricular or cortical, and the brains were analyzed at 4 and 8 week post-transplantation (Figures S7A–S7G). In all experimental groups, immunohistochemical analysis revealed strong immunoreactivity for the human cytoplasm marker (STEM121) at the injection sites as well different brains regions in the ipsi- and contralateral hemispheres. Migratory astrocytes co-expressing human-specific GFAP (hGFAP; STEM123 antibody) and S100B were widely distributed and detectable in the cortex (Figure S7B), corpus callosum (Figure S7C), hippocampus (Figure S7D), thalamus (Figure S7E), and blood vessels in the brain parenchyma (Figure S7F). Quantitative analysis showed that the highest number of transplanted human astrocytes was detected in neonatal animals 8 weeks post grafting (Figure S7G). These experiments demonstrated that hPSC-derived astrocytes engraft, migrate over long distances, and survive *in vivo* for several weeks.

Figure 7. Robotic biomanufacturing of human astrocytes for disease modeling

(A) iPSC-derived astrocytes (S100B$^+$, GFAP$^+$) from an Alexander disease (AxD) patient (GM16825) and an unaffected individual (non-isogenic control, NCRM5).

(B) AxD astrocytes showing typical GFAP$^+$ protein aggregates and aberrant morphology.

(C) Electron microscopy of AxD astrocytes (day 50). Note the dark electron-dense material representing Rosenthal fibers.

(D) Electron micrograph of a multi-lamellar body. Note the multi-lamellar structure surrounding organelles that are being digested. A red arrow indicates mitochondria entering the lysosome (blue arrow).

(E) Black arrows indicate enlarged ER.

(F) Western blot showing elevated expression of markers for ER stress and autophagy. Note that total expression of TDP-43 is higher in AxD astrocytes versus control.

(G) Seahorse glycolysis stress testing glycolytic flux in AxD patient astrocytes and control astrocytes cultured under regular conditions (Astro-3 medium). Glycolytic flux is measured as extracellular acidification rate (ECAR). Data are normalized to total cell numbers per well. n = 6 replicate wells per condition. Control (NCRM5), AxD patient (GM16825).

(H) Glycolysis stress test after 24-h exposure to inflammatory cytokines (TNF-α, C1Q, and IL-1a). Note the decreased glycolysis, measured after glucose administration, and total glycolytic capacity, measured after oligomycin administration to block mitochondrial respiration, compared control astrocytes. n = 6 replicate wells per condition. Control (NCRM5), AxD patient (GM16825).

(I) Schematic of the robotic workflow and scalable astrocyte production using the CompacT SelecT platform (Sartorius) suitable for translational applications.

All data are presented as mean ± SD. Scale bars, 100 μm (A and B) and 500 nm (C–E).

Last, clinically relevant protocols should enable large-scale biomanufacturing of human cells from hPSCs. We therefore automated our scalable astrocyte differentiation protocol using the CompacT SelecT robotic cell culture platform (Figure 7I). This approach, in combination with the CEPT small-molecule cocktail (Chen et al., 2021), enabled the routine production of up to 500 million astrocytes in a single manufacturing workflow, and astrocytes could be cryopreserved on day 30 and used on demand for various applications.

DISCUSSION

During development, the neural lineage generates the three major cell types in a highly coordinated sequential fashion: neurons, astrocytes, and oligodendrocytes (Rowitch and Kriegstein, 2010). Astrocytes play crucial roles in the normal and diseased human brain, but the precise mechanisms of glial cell fate choice and differentiation remain poorly understood. Here, we established a novel strategy that differentiates hPSCs into RGCs and then directly into astrocytes, obviating neurogenesis and oligodendrogenesis. This stepwise method is based on bone morphogenetic protein (BMP) inhibition and activation of gliogenic pathways (Deverman and Patterson, 2009; Namihira et al., 2009). Our study has several far-reaching implications. First, generation of RGCs with improved capability for neural rosette formation and transcriptomic similarity to resident RGCs of the human fetal telencephalon (Nowakowski et al., 2017) should leverage future studies. RGCs were responsive to rostro-caudal patterning cues and produced neurons and OLIG2-expressing cells under different culture conditions. Therefore, generation of *bona fide* RGCs could become an alternative to dSMADi (Chambers et al., 2009) and applied to more faithfully recapitulate CNS development *in vitro*.

Second, if highly controlled RGC differentiation into astrocytes is employed, then strong NFIA expression is obtained on day 21 without long-term expansion of NPCs or genetic manipulation (Tchieu et al., 2019). As one of the contributing mechanisms for gliogenesis, we suggest an activated EGF pathway in the absence of recombinant EGF. Alternative culture conditions, including recombinant EGF/FGF2 administration, promoted neurogenesis and suppressed NFIA expression. Adding FBS to Astro-1/Astro-2 medium induced expression of histone genes, similar to a signature found in human fetal astrocytes. Considering that FBS can contribute to cell maturation or result in reactive astrocytes and that histone genes are involved in various molecular processes (Burda et al., 2022), future work is necessary to elucidate these findings. Our approach confirmed a direct RGC-to-astrocyte differentiation model at the expense of neurogenesis. The chromatin state and expression of SOX9, NFIA, NFIB, and REST and absence of neurogenic genes (e.g., NEUROG1/2/3) across different time points was consistent with exclusive astrogliogenesis. Previous single-cell studies of mouse and human brain development have mapped early cortical neurogenesis and neuronal subtype specification (Di Bella et al., 2021; Eze et al., 2021), whereas differentiation trajectories of human RGCs and early glial specification remain understudied. Hence, our multi-omics datasets represent an invaluable resource for studying human gliogenesis.

Third, derived astrocytes remain immature relative to primary astrocytes from adult brains, which is consistent with previous reports (Canals et al., 2018; Krencik et al., 2011; Li et al., 2018b; Santos et al., 2017; Tchieu et al., 2019; Tcw et al., 2017). Our findings suggest potential important roles for *NCOR-2*, *SYNJ2*, and *DLG5* in astrocyte maturation. Finally, our demonstration of industrial-scale production of patient- and disease-specific astrocytes may help to deliver on the promise of iPSCs and leverage drug development and personalized therapies for neurological and psychiatric illnesses.

EXPERIMENTAL PROCEDURES

Resource availability

Corresponding author

Further information and requests for resources and reagents should be directed to and will be fulfilled by the corresponding authors: Vukasin Jovanovic (vukasin.jovanovic@nih.gov) and Ilyas Singeç (ilyassingec@gmail.com).

Materials availability

All materials and reagents generated in this study will be made available upon request following NIH guidelines.

Data and code availability

Data are presented as the mean ± SD. Statistical analyses (GraphPad Prism) were performed using different tests as appropriate and as described in the figure legends.

Bulk RNA-seq and scRNA-seq, ATAC-seq, and MeDIP-seq FASTQ files have been deposited into the Sequence Read Archive (SRA) under BioProject PRJNA769413. The code for sequencing data analysis is available at https://github.com/cemalley/Jovanovic_methods and https://github.com/jaro-slamecka/Jovanovic_astrocyte_scRNA-seq. Public databases used include Gene Ontology 2019 (http://geneontology.org/), ARCHS4 Tissues (https://maayanlab.cloud/archs4/), and UCSC Cell Browser (https://cells.ucsc.edu/?ds=cortex-dev). Public SRA datasets used were PRJNA412090, PRJNA382448, PRJNA383243, and PRJNA297760.

Cell culture

The hESCs line (WA09), healthy donor iPSC lines (LiPSC-GR1.1, GM25256 [WTC11], and NCRM5 from the NIH Common Fund), and patient-derived AxD iPSCs (GM16825, Coriell) were

maintained under feeder-free conditions using E8 medium and VN-coated plates (Thermo Fisher Scientific, A14700). Cells were routinely passaged using 0.5 mM EDTA diluted in phosphate-buffered saline (PBS) without calcium or magnesium (Thermo Fisher Scientific) when culture plates reached about 70%–90% confluency, typically every 3–4 days. For the initial 24 h after cell passaging, E8 medium was supplemented with the CEPT cocktail to optimize cell viability (Chen et al., 2021).

Astrocyte differentiation using Astro-1, Astro-2, and Astro-3 media

Astro-1 medium was composed of DMEM/F12 medium supplemented with N2 (Gibco, 17502048), B27 without vitamin A (Gibco, 12587010), 100 nM LDN-193189 dihydrochloride (Tocris, 6053), and the human recombinant proteins PDGF-AA (R&D Systems, 221-AA), JAGGED-1 (R&D Systems, 1277-JG), DLL-1 (R&D Systems, 1818-DL), ONCOSTATIN M (R&D Systems, 295-OM), LIF (R&D Systems, 7734-LF), and CNTF (R&D Systems, 257-NT) (all at 10 ng/mL concentration).

Astro-2 medium was composed of DMEM/F12 base medium supplemented with N2 (Gibco), B27 complete (Gibco, 17504044), 1% lipid supplement (Gibco, 11905031), and the recombinant proteins JAGGED1, DLL-1, ONCOSTATIN M, LIF, and CNTF (all at 10 ng/mL concentration) (R&D Systems).

Astro-3 medium was composed of DMEM/F12 base medium supplemented with N2, B27 with vitamin A, 1% lipid supplement (Gibco), and JAGGED1, DLL-1, LIF, CNTF (all at 10 ng/mL concentration), hNRG1/EGF domain (20 ng/mL, R&D Systems, 396-HB), 2 μM forskolin (Tocris, 1099), 200 nM phorbol-12 myristate-13 acetate (Tocris, 1201), 40 ng/mL triiodothyronine T3 (Tocris, 6666), and 200 μM ascorbic acid (Tocris, 4055).

SUPPLEMENTAL INFORMATION

Supplemental information can be found online at https://doi.org/10.1016/j.stemcr.2023.06.007.

AUTHOR CONTRIBUTIONS

V.M.J. and I.S. conceived the project. Experiments, V.M.J., C.S., C.A.T., S.R., P.-H.C., E.B., P.O., J.C.M., S.M., Y.J., J.F.D.S ; data analysis and discussions, V.M.J., J.S., C.W., J.I., M.H., D.G., T.C.V., C.A.T., M.E.W., A.S., and I.S.; manuscript writing, V.M.J. and I.S.

ACKNOWLEDGMENTS

We thank H. Hong, P. Francis, T. Deng, J. Freilino, M. Iannotti, C. Pepper Bonney, Y. Gedik, D. Ngan, and H. Baskir for support. We are grateful to A. Hoofring from the NIH Medical Arts Design Section for art designs, K. Nagashima from the Electron Microscopy Laboratory at the National Cancer Institute (NCI) for electron microscopy images, and D. Havas (PsychoGenics) for confocal microscopy and quantification of grafted cells. We also acknowledge funding from the Regenerative Medicine Program (RMP) of the NIH Common Fund and in part by the intramural research program of the National Center for Advancing Translational Sciences (NCATS), NIH. The funders had no role in study design, data collection, and analysis; decision to publish; or preparation of the manuscript.

CONFLICT OF INTERESTS

V.M.J., A.S., and I.S. are coinventors on a US Department of Health and Human Services patent covering the described radial glia and astrocyte differentiation method and its use.

Received: August 11, 2022
Revised: June 14, 2023
Accepted: June 15, 2023
Published: July 13, 2023

REFERENCES

Badouel, C., Zander, M.A., Liscio, N., Bagherie-Lachidan, M., Sopko, R., Coyaud, E., Raught, B., Miller, F.D., and McNeill, H. (2015). Fat1 interacts with Fat4 to regulate neural tube closure, neural progenitor proliferation and apical constriction during mouse brain development. Development *142*, 2781–2791. https://doi.org/10.1242/dev.123539.

Ballas, N., Grunseich, C., Lu, D.D., Speh, J.C., and Mandel, G. (2005). REST and its corepressors mediate plasticity of neuronal gene chromatin throughout neurogenesis. Cell *121*, 645–657. https://doi.org/10.1016/j.cell.2005.03.013.

Baskin, R., Woods, N.T., Mendoza-Fandiño, G., Forsyth, P., Egan, K.M., and Monteiro, A.N.A. (2015). Functional analysis of the 11q23.3 glioma susceptibility locus implicates PHLDB1 and DDX6 in glioma susceptibility. Sci. Rep. *5*, 17367. https://doi.org/10.1038/srep17367.

Brenner, M., Johnson, A.B., Boespflug-Tanguy, O., Rodriguez, D., Goldman, J.E., and Messing, A. (2001). Mutations in GFAP, encoding glial fibrillary acidic protein, are associated with Alexander disease. Nat. Genet. *27*, 117–120. https://doi.org/10.1038/83679.

Burda, J.E., O'Shea, T.M., Ao, Y., Suresh, K.B., Wang, S., Bernstein, A.M., Chandra, A., Deverasetty, S., Kawaguchi, R., Kim, J.H., et al. (2022). Divergent transcriptional regulation of astrocyte reactivity across disorders. Nature *606*, 557–564. https://doi.org/10.1038/s41586-022-04739-5.

Burrows, R.C., Wancio, D., Levitt, P., and Lillien, L. (1997). Response diversity and the timing of progenitor cell maturation are regulated by developmental changes in EGFR expression in the cortex. Neuron *19*, 251–267. https://doi.org/10.1016/s0896-6273(00)80937-x.

Caiazzo, M., Giannelli, S., Valente, P., Lignani, G., Carissimo, A., Sessa, A., Colasante, G., Bartolomeo, R., Massimino, L., Ferroni, S., et al. (2015). Direct conversion of fibroblasts into functional astrocytes by defined transcription factors. Stem Cell Rep. *4*, 25–36. https://doi.org/10.1016/j.stemcr.2014.12.002.

Canals, I., Ginisty, A., Quist, E., Timmerman, R., Fritze, J., Miskinyte, G., Monni, E., Hansen, M.G., Hidalgo, I., Bryder, D., et al. (2018). Rapid and efficient induction of functional astrocytes from human pluripotent stem cells. Nat. Methods *15*, 693–696. https://doi.org/10.1038/s41592-018-0103-2.

Chambers, S.M., Fasano, C.A., Papapetrou, E.P., Tomishima, M., Sadelain, M., and Studer, L. (2009). Highly efficient neural conversion of human ES and iPS cells by dual inhibition of SMAD signaling. Nat. Biotechnol. *27*, 275–280. https://doi.org/10.1038/nbt.1529.

Chen, Y., Tristan, C.A., Chen, L., Jovanovic, V.M., Malley, C., Chu, P.H., Ryu, S., Deng, T., Ormanoglu, P., Tao, D., et al. (2021). A versatile polypharmacology platform promotes cytoprotection and viability of human pluripotent and differentiated cells. Nat. Methods *18*, 528–541. https://doi.org/10.1038/s41592-021-01126-2.

Cohen, D.R., Cheng, C.W., Cheng, S.H., and Hui, C.C. (2000). Expression of two novel mouse Iroquois homeobox genes during neurogenesis. Mech. Dev. *91*, 317–321. https://doi.org/10.1016/s0925-4773(99)00263-4.

Deneen, B., Ho, R., Lukaszewicz, A., Hochstim, C.J., Gronostajski, R.M., and Anderson, D.J. (2006). The transcription factor NFIA controls the onset of gliogenesis in the developing spinal cord. Neuron *52*, 953–968. https://doi.org/10.1016/j.neuron.2006.11.019.

Deverman, B.E., and Patterson, P.H. (2009). Cytokines and CNS development. Neuron *64*, 61–78. https://doi.org/10.1016/j.neuron.2009.09.002.

Di Bella, D.J., Habibi, E., Stickels, R.R., Scalia, G., Brown, J., Yadollahpour, P., Yang, S.M., Abbate, C., Biancalani, T., Macosko, E.Z., et al. (2021). Author Correction: Molecular logic of cellular diversification in the mouse cerebral cortex. Nature *596*, E11. https://doi.org/10.1038/s41586-021-03797-5.

Elkabetz, Y., Panagiotakos, G., Al Shamy, G., Socci, N.D., Tabar, V., and Studer, L. (2008). Human ES cell-derived neural rosettes reveal a functionally distinct early neural stem cell stage. Genes Dev. *22*, 152–165. https://doi.org/10.1101/gad.1616208.

Eze, U.C., Bhaduri, A., Haeussler, M., Nowakowski, T.J., and Kriegstein, A.R. (2021). Single-cell atlas of early human brain development highlights heterogeneity of human neuroepithelial cells and early radial glia. Nat. Neurosci. *24*, 584–594. https://doi.org/10.1038/s41593-020-00794-1.

Fernandopulle, M.S., Prestil, R., Grunseich, C., Wang, C., Gan, L., and Ward, M.E. (2018). Transcription factor-mediated differentiation of human iPSCs into neurons. Curr. Protoc. Cell Biol. *79*, e51. https://doi.org/10.1002/cpcb.51.

Fish, J.L., Kosodo, Y., Enard, W., Pääbo, S., and Huttner, W.B. (2006). Aspm specifically maintains symmetric proliferative divisions of neuroepithelial cells. Proc. Natl. Acad. Sci. USA *103*, 10438–10443. https://doi.org/10.1073/pnas.0604066103.

García-Marín, V., García-López, P., and Freire, M. (2007). Cajal's contributions to glia research. Trends Neurosci. *30*, 479–487. https://doi.org/10.1016/j.tins.2007.06.008.

Hirabayashi, Y., Suzki, N., Tsuboi, M., Endo, T.A., Toyoda, T., Shinga, J., Koseki, H., Vidal, M., and Gotoh, Y. (2009). Polycomb limits the neurogenic competence of neural precursor cells to promote astrogenic fate transition. Neuron *63*, 600–613. https://doi.org/10.1016/j.neuron.2009.08.021.

Hogea, A., Shah, S., Jones, F., Carver, C.M., Hao, H., Liang, C., Huang, D., Du, X., and Gamper, N. (2021). Junctophilin-4 facilitates inflammatory signalling at plasma membrane-endoplasmic reticulum junctions in sensory neurons. J. Physiol. *599*, 2103–2123. https://doi.org/10.1113/jp281331.

Hung, A.Y., Futai, K., Sala, C., Valtschanoff, J.G., Ryu, J., Woodworth, M.A., Kidd, F.L., Sung, C.C., Miyakawa, T., Bear, M.F., et al. (2008). Smaller dendritic spines, weaker synaptic transmission, but enhanced spatial learning in mice lacking Shank1. J. Neurosci. *28*, 1697–1708. https://doi.org/10.1523/jneurosci.3032-07.2008.

Jaillard, C., Harrison, S., Stankoff, B., Aigrot, M.S., Calver, A.R., Duddy, G., Walsh, F.S., Pangalos, M.N., Arimura, N., Kaibuchi, K., et al. (2005). Edg8/S1P5: an oligodendroglial receptor with dual function on process retraction and cell survival. J. Neurosci. *25*, 1459–1469. https://doi.org/10.1523/jneurosci.4645-04.2005.

Jiang, Y., de Bruin, A., Caldas, H., Fangusaro, J., Hayes, J., Conway, E.M., Robinson, M.L., and Altura, R.A. (2005). Essential role for survivin in early brain development. J. Neurosci. *25*, 6962–6970. https://doi.org/10.1523/jneurosci.1446-05.2005.

Jones, J.R., Kong, L., Hanna, M.G., 4th, Hoffman, B., Krencik, R., Bradley, R., Hagemann, T., Choi, J., Doers, M., Dubovis, M., et al. (2018). Mutations in GFAP disrupt the distribution and function of organelles in human astrocytes. Cell Rep. *25*, 947–958.e4. https://doi.org/10.1016/j.celrep.2018.09.083.

Junghans, D., and Herzog, S. (2018). Cnn3 regulates neural tube morphogenesis and neuronal stem cell properties. FEBS J. *285*, 325–338. https://doi.org/10.1111/febs.14338.

Kang, P., Lee, H.K., Glasgow, S.M., Finley, M., Donti, T., Gaber, Z.B., Graham, B.H., Foster, A.E., Novitch, B.G., Gronostajski, R.M., and Deneen, B. (2012). Sox9 and NFIA coordinate a transcriptional regulatory cascade during the initiation of gliogenesis. Neuron *74*, 79–94. https://doi.org/10.1016/j.neuron.2012.01.024.

Krencik, R., Weick, J.P., Liu, Y., Zhang, Z.J., and Zhang, S.C. (2011). Specification of transplantable astroglial subtypes from human pluripotent stem cells. Nat. Biotechnol. *29*, 528–534. https://doi.org/10.1038/nbt.1877.

Lachmann, A., Torre, D., Keenan, A.B., Jagodnik, K.M., Lee, H.J., Wang, L., Silverstein, M.C., and Ma'ayan, A. (2018). Massive mining of publicly available RNA-seq data from human and mouse. Nat. Commun. *9*, 1366. https://doi.org/10.1038/s41467-018-03751-6.

Lager, A.M., Corradin, O.G., Cregg, J.M., Elitt, M.S., Shick, H.E., Clayton, B.L.L., Allan, K.C., Olsen, H.E., Madhavan, M., and Tesar, P.J. (2018). Rapid functional genetics of the oligodendrocyte lineage using pluripotent stem cells. Nat. Commun. *9*, 3708. https://doi.org/10.1038/s41467-018-06102-7.

Leventoux, N., Morimoto, S., Imaizumi, K., Sato, Y., Takahashi, S., Mashima, K., Ishikawa, M., Sonn, I., Kondo, T., Watanabe, H., and Okano, H. (2020). Human astrocytes model derived from induced pluripotent stem cells. Cells *9*, 2680. https://doi.org/10.3390/cells9122680.

Li, J., Sun, L., Peng, X.L., Yu, X.M., Qi, S.J., Lu, Z.J., Han, J.D.J., and Shen, Q. (2021). Integrative genomic analysis of early neurogenesis reveals a temporal genetic program for differentiation and specification of preplate and Cajal-Retzius neurons. PLoS Genet. *17*, e1009355. https://doi.org/10.1371/journal.pgen.1009355.

Li, L., Tian, E., Chen, X., Chao, J., Klein, J., Qu, Q., Sun, G., Sun, G., Huang, Y., Warden, C.D., et al. (2018a). GFAP mutations in astrocytes impair oligodendrocyte progenitor proliferation and myelination in an hiPSC model of Alexander disease. Cell Stem Cell *23*, 239–251.e6. https://doi.org/10.1016/j.stem.2018.07.009.

Li, X., Tao, Y., Bradley, R., Du, Z., Tao, Y., Kong, L., Dong, Y., Jones, J., Yan, Y., Harder, C.R.K., et al. (2018b). Fast generation of functional subtype astrocytes from human pluripotent stem cells. Stem Cell Rep. *11*, 998–1008. https://doi.org/10.1016/j.stemcr.2018.08.019.

Liddelow, S.A., Guttenplan, K.A., Clarke, L.E., Bennett, F.C., Bohlen, C.J., Schirmer, L., Bennett, M.L., Münch, A.E., Chung, W.S., Peterson, T.C., et al. (2017). Neurotoxic reactive astrocytes are induced by activated microglia. Nature *541*, 481–487. https://doi.org/10.1038/nature21029.

Lunyak, V.V., and Rosenfeld, M.G. (2005). No rest for REST: REST/NRSF regulation of neurogenesis. Cell *121*, 499–501. https://doi.org/10.1016/j.cell.2005.05.003.

Marton, R.M., Miura, Y., Sloan, S.A., Li, Q., Revah, O., Levy, R.J., Huguenard, J.R., and Pașca, S.P. (2019). Differentiation and maturation of oligodendrocytes in human three-dimensional neural cultures. Nat. Neurosci. *22*, 484–491. https://doi.org/10.1038/s41593-018-0316-9.

Molofsky, A.V., Krencik, R., Ullian, E.M., Tsai, H.H., Deneen, B., Richardson, W.D., Barres, B.A., and Rowitch, D.H. (2012). Astrocytes and disease: a neurodevelopmental perspective. Genes Dev. *26*, 891–907. https://doi.org/10.1101/gad.188326.112.

Murai, K., Philpott, A., and Jones, P.H. (2011). Hes6 is required for the neurogenic activity of neurogenin and NeuroD. PLoS One *6*, e27880. https://doi.org/10.1371/journal.pone.0027880.

Naka, H., Nakamura, S., Shimazaki, T., and Okano, H. (2008). Requirement for COUP-TFI and II in the temporal specification of neural stem cells in CNS development. Nat. Neurosci. *11*, 1014–1023. https://doi.org/10.1038/nn.2168.

Namihira, M., Kohyama, J., Semi, K., Sanosaka, T., Deneen, B., Taga, T., and Nakashima, K. (2009). Committed Neuronal Precursors Confer Astrocytic Potential on Residual Neural Precursor Cells. Dev. Cell. *16*, 245–255.

Noctor, S.C., Flint, A.C., Weissman, T.A., Dammerman, R.S., and Kriegstein, A.R. (2001). Neurons derived from radial glial cells establish radial units in neocortex. Nature *409*, 714–720. https://doi.org/10.1038/35055553.

Nowakowski, T.J., Bhaduri, A., Pollen, A.A., Alvarado, B., Mostajo-Radji, M.A., Di Lullo, E., Haeussler, M., Sandoval-Espinosa, C., Liu, S.J., Velmeshev, D., et al. (2017). Spatiotemporal gene expression trajectories reveal developmental hierarchies of the human cortex. Science *358*, 1318–1323. https://doi.org/10.1126/science.aap8809.

Rowitch, D.H., and Kriegstein, A.R. (2010). Developmental genetics of vertebrate glial-cell specification. Nature *468*, 214–222. https://doi.org/10.1038/nature09611.

Santos, R., Vadodaria, K.C., Jaeger, B.N., Mei, A., Lefcochilos-Fogelquist, S., Mendes, A.P.D., Erikson, G., Shokhirev, M., Randolph-Moore, L., Fredlender, C., et al. (2017). Differentiation of inflammation-responsive astrocytes from glial progenitors generated from human induced pluripotent stem cells. Stem Cell Rep. *8*, 1757–1769. https://doi.org/10.1016/j.stemcr.2017.05.011.

Schmechel, D.E., and Rakic, P. (1979). Arrested proliferation of radial glial cells during midgestation in rhesus monkey. Nature *277*, 303–305. https://doi.org/10.1038/277303a0.

Sherwood, M.W., Arizono, M., Panatier, A., Mikoshiba, K., and Oliet, S.H.R. (2021). Astrocytic IP(3)Rs: Beyond IP(3)R2. Front. Cell. Neurosci. *15*, 695817. https://doi.org/10.3389/fncel.2021.695817.

Shi, Y., Lan, F., Matson, C., Mulligan, P., Whetstine, J.R., Cole, P.A., Casero, R.A., and Shi, Y. (2004). Histone demethylation mediated by the nuclear amine oxidase homolog LSD1. Cell *119*, 941–953. https://doi.org/10.1016/j.cell.2004.12.012.

Sloan, S.A., and Barres, B.A. (2014). Mechanisms of astrocyte development and their contributions to neurodevelopmental disorders. Curr. Opin. Neurobiol. *27*, 75–81. https://doi.org/10.1016/j.conb.2014.03.005.

Sloan, S.A., Darmanis, S., Huber, N., Khan, T.A., Birey, F., Caneda, C., Reimer, R., Quake, S.R., Barres, B.A., and Pașca, S.P. (2017). Human astrocyte maturation captured in 3D cerebral cortical spheroids derived from pluripotent stem cells. Neuron *95*, 779–790.e6. https://doi.org/10.1016/j.neuron.2017.07.035.

Street, K., Risso, D., Fletcher, R.B., Das, D., Ngai, J., Yosef, N., Purdom, E., and Dudoit, S. (2018). Slingshot: cell lineage and pseudotime inference for single-cell transcriptomics. BMC Genom. *19*, 477. https://doi.org/10.1186/s12864-018-4772-0.

Sun, Y., Nadal-Vicens, M., Misono, S., Lin, M.Z., Zubiaga, A., Hua, X., Fan, G., and Greenberg, M.E. (2001). Neurogenin promotes neurogenesis and inhibits glial differentiation by independent mechanisms. Cell *104*, 365–376. https://doi.org/10.1016/s0092-8674(01)00224-0.

Tchieu, J., Calder, E.L., Guttikonda, S.R., Gutzwiller, E.M., Aromolaran, K.A., Steinbeck, J.A., Goldstein, P.A., and Studer, L. (2019). NFIA is a gliogenic switch enabling rapid derivation of functional human astrocytes from pluripotent stem cells. Nat. Biotechnol. *37*, 267–275. https://doi.org/10.1038/s41587-019-0035-0.

Tcw, J., Wang, M., Pimenova, A.A., Bowles, K.R., Hartley, B.J., Lacin, E., Machlovi, S.I., Abdelaal, R., Karch, C.M., Phatnani, H., et al. (2017). An efficient platform for astrocyte differentiation from human induced pluripotent stem cells. Stem Cell Rep. *9*, 600–614. https://doi.org/10.1016/j.stemcr.2017.06.018.

Van den Berge, K., Roux de Bézieux, H., Street, K., Saelens, W., Cannoodt, R., Saeys, Y., Dudoit, S., and Clement, L. (2020). Trajectory-based differential expression analysis for single-cell sequencing data. Nat. Commun. *11*, 1201. https://doi.org/10.1038/s41467-020-14766-3.

Velasco, S., Kedaigle, A.J., Simmons, S.K., Nash, A., Rocha, M., Quadrato, G., Paulsen, B., Nguyen, L., Adiconis, X., Regev, A., et al. (2019). Individual brain organoids reproducibly form cell diversity of the human cerebral cortex. Nature *570*, 523–527. https://doi.org/10.1038/s41586-019-1289-x.

Verkhratsky, A., and Kettenmann, H. (1996). Calcium signalling in glial cells. Trends Neurosci. *19*, 346–352. https://doi.org/10.1016/0166-2236(96)10048-5.

Wilton, D.K., Dissing-Olesen, L., and Stevens, B. (2019). Neuron-Glia signaling in synapse elimination. Annu. Rev. Neurosci. *42*, 107–127. https://doi.org/10.1146/annurev-neuro-070918-050306.

Zhang, Y., Sloan, S.A., Clarke, L.E., Caneda, C., Plaza, C.A., Blumenthal, P.D., Vogel, H., Steinberg, G.K., Edwards, M.S.B., Li, G., et al. (2016). Purification and characterization of progenitor and mature

human astrocytes reveals transcriptional and functional differences with mouse. Neuron *89*, 37–53. https://doi.org/10.1016/j.neuron.2015.11.013.

Zhu, Q., Chen, L., Li, Y., Huang, M., Shao, J., Li, S., Cheng, J., Yang, H., Wu, Y., Zhang, J., et al. (2021). Rack1 is essential for corticogenesis by preventing p21-dependent senescence in neural stem cells. Cell Rep. *36*, 109639. https://doi.org/10.1016/j.celrep.2021.109639.

Zuchero, J.B., and Barres, B.A. (2015). Glia in mammalian development and disease. Development *142*, 3805–3809. https://doi.org/10.1242/dev.129304.

Stem Cell Reports, Volume *18*

Supplemental Information

A defined roadmap of radial glia and astrocyte differentiation from human pluripotent stem cells

Vukasin M. Jovanovic, Claire Weber, Jaroslav Slamecka, Seungmi Ryu, Pei-Hsuan Chu, Chaitali Sen, Jason Inman, Juliana Ferreira De Sousa, Elena Barnaeva, Marissa Hirst, David Galbraith, Pinar Ormanoglu, Yogita Jethmalani, Jennifer Colon Mercado, Sam Michael, Michael E. Ward, Anton Simeonov, Ty C. Voss, Carlos A. Tristan, and Ilyas Singeç

Supplemental Information (Jovanovic et al.)

Figure S1

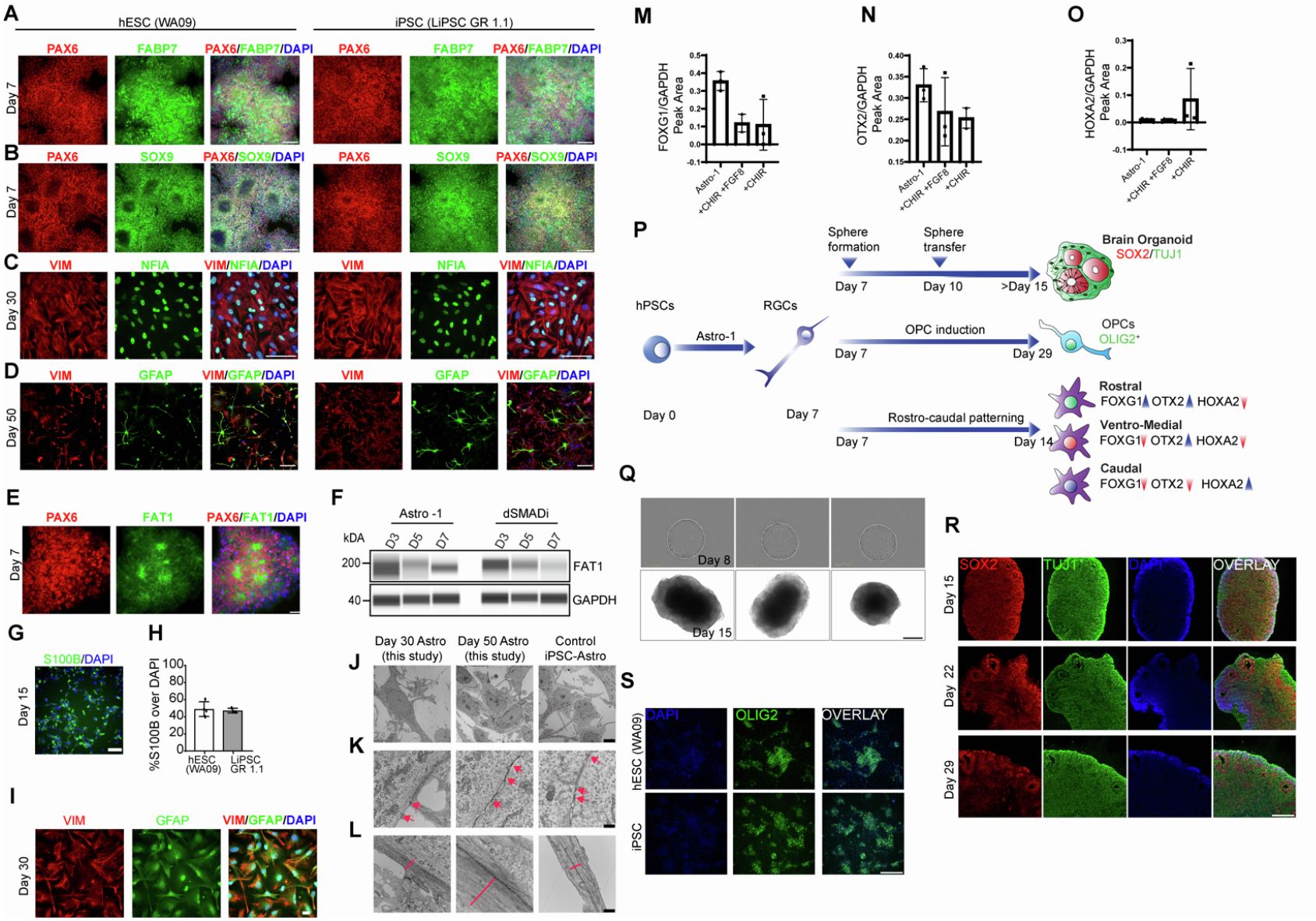

Figure S1. Reproducible generation and specification of multipotent RGCs

(A, B) Neural rosettes expressing PAX6, FABP7, and SOX9 after hPSCs (WA09 and LiPSC-GR1.1) were treated with Astro-1 medium for 7 days.

(C) Representative images showing nuclear NFIA expression in the majority of cells (day 30).

(D) Astrocytes expressing GFAP and VIM (day 50). Scale bars, 100 μm.

(E) Immunostaining showing FAT1 expression by neural rosettes.

(F) Western blot showing differences in FAT1 expression during neural induction with Astro-1 versus dSMADi.

(G) Immunocytochemistry for S100B in differentiating cultures (day 15).

(H) Quantification of S100B$^+$ cells (day 15). Data expressed as mean ± SD. n = 4 replicate wells for 2 independent cell lines (WA09, LiPSC GR 1.1).

(I) Diffuse immunoreactivity for GFAP in immature astrocytes (day 30).

(J) Electron microscopy showing typical stellate morphology of astrocytes (LiPSC-GR1.1).

(K) Astrocytes showing prominent tight junctions (red arrowheads).

(L) Astrocytic processes (red dashed lines) with abundant intermediate filaments.

(M-O) Quantitative immunoblotting after rostro-caudal patterning of RGCs demonstrating (M) downregulation of FOXG1 in response to WNT pathway activation and FGF8 administration, or WNT activation alone, (N) reduction of OTX2 expression and (O) Upregulation of HOXA2 in response to WNT activation. Each bar graph represents replicates from WA09, LiPSC GR1.1, and NCRM5.

(P) Experimental design for RGC patterning. RGCs were used to generate spheroids based on a previously published protocol (Marton et al., 2019), patterned in monolayer cultures by including SAG21K, EGF/FGF2 and RA to Astro-1 medium to generate OLIG2$^+$ progenitors, or WNT activation (CHIR99021) with and without FGF8 for caudalization (see Experimental Procedures).

(Q) Phase contrast images of RGC-derived spheroids at day 8 (24 h after spheroid formation) and day 15 (WA09).

(R) Immunohistochemistry of sectioned spheroids (day 15, 22, 29) showing neural tube-like structures with SOX2$^+$ cells surrounded by TUJ1$^+$ neurons. Note the time-dependent decrease of SOX2$^+$ cells. Scale bars 100 μm.

(S) Immunocytochemistry showing OLIG2 expression in RGCs after treatment with EGF/FGF2/SAG21k/RA over the course of 21 days. Experiments were independently reproduced with WA09 and LiPSC GR 1.1 lines. Scale bars, (A-E, I) 100 μm, (J) 10 μm, (K, L) 0.5 μm, (Q) 300 μm, (S) 100 μm.

Figure S2

A

Treatment condition	Day 0 - 7	Day 7 - 14	Day 14 -21	Sample Collection
1	BMPi	BMPi	Astro-2	Day 21
2	dSMADi	EGF/FGF	EGF/FGF	Day 21
3	Astro-1	Astro-1	Astro-2	Day 21
4	Astro-1 + FGF/EGF	Astro-1 + FGF/EGF	Astro-2 + EGF/FGF	Day 21
5	Astro-1	Astro-1	Astro-2 + EGFi/FGFi (PD17/Afatinib)	Day 21
6	Astro-1 - NOTCH	Astro-1 - NOTCH	Astro-2 - NOTCH (Jagged-1/DLL-1)	Day 21

B

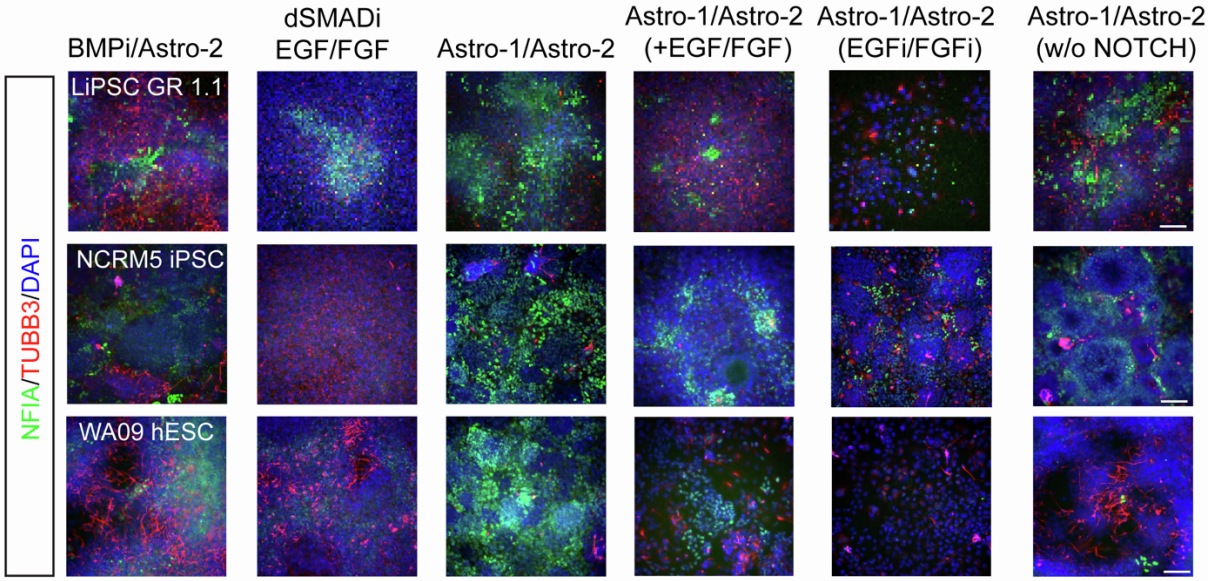

C

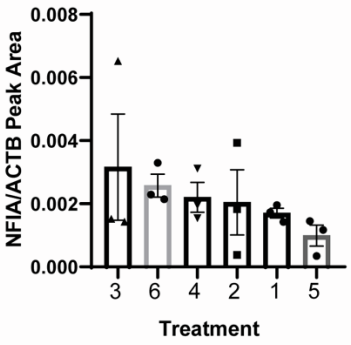

D

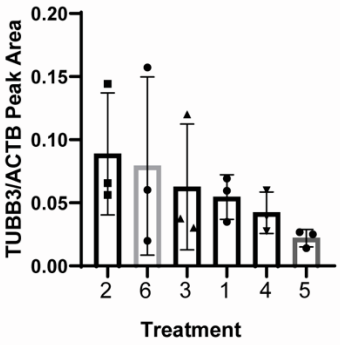

E

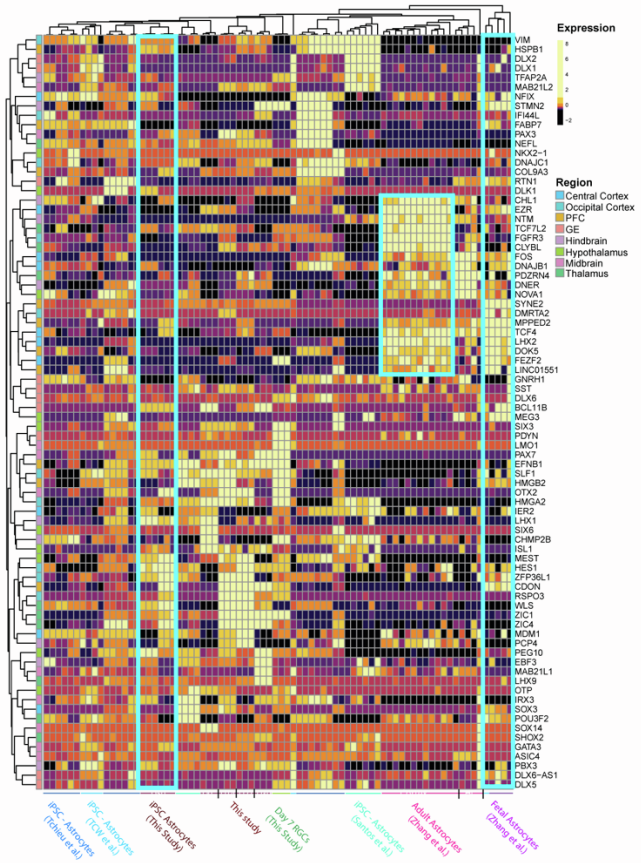

Figure S2. Characterization of Astro-1/Astro-2 media for NFIA induction and regional identity of RGCs and astrocytes.

(A) Table summarizing the treatment combinations tested over the course of 21 days. For more details see Experimental Procedures.

(B) Immunocytochemistry showing NFIA and TUBB3 expression (day 21) after differentiating 3 different cell lines (WA09, LiPSC GR 1.1, NCRM5) subjected to 6 different treatment conditions.

(C-D) Quantitative immunoblotting of NFIA and TUBB3 expression. Note the strongest average expression of NFIA with Astro-1/Astro 2 (treatment #3), and the strongest TUBB3 expression in cultures treated with dSMADi followed by cell expansion with EGF/FGF2 (treatment group #2). Experimental design and treatment groups shown in (A).

(E) Heatmap of clustering analysis for regional gene markers across samples of iPSC-derived RGCs and astrocytes from this study as well as previously published studies and comparison to primary human adult astrocytes (cortex and hippocampus) and primary human fetal astrocytes (cortex). Note the lack of regional identity in fetal astrocytes and iPSC-derived astrocytes as compared to adult human astrocytes.

Scale bars (B) 100 μm.

Figure S3

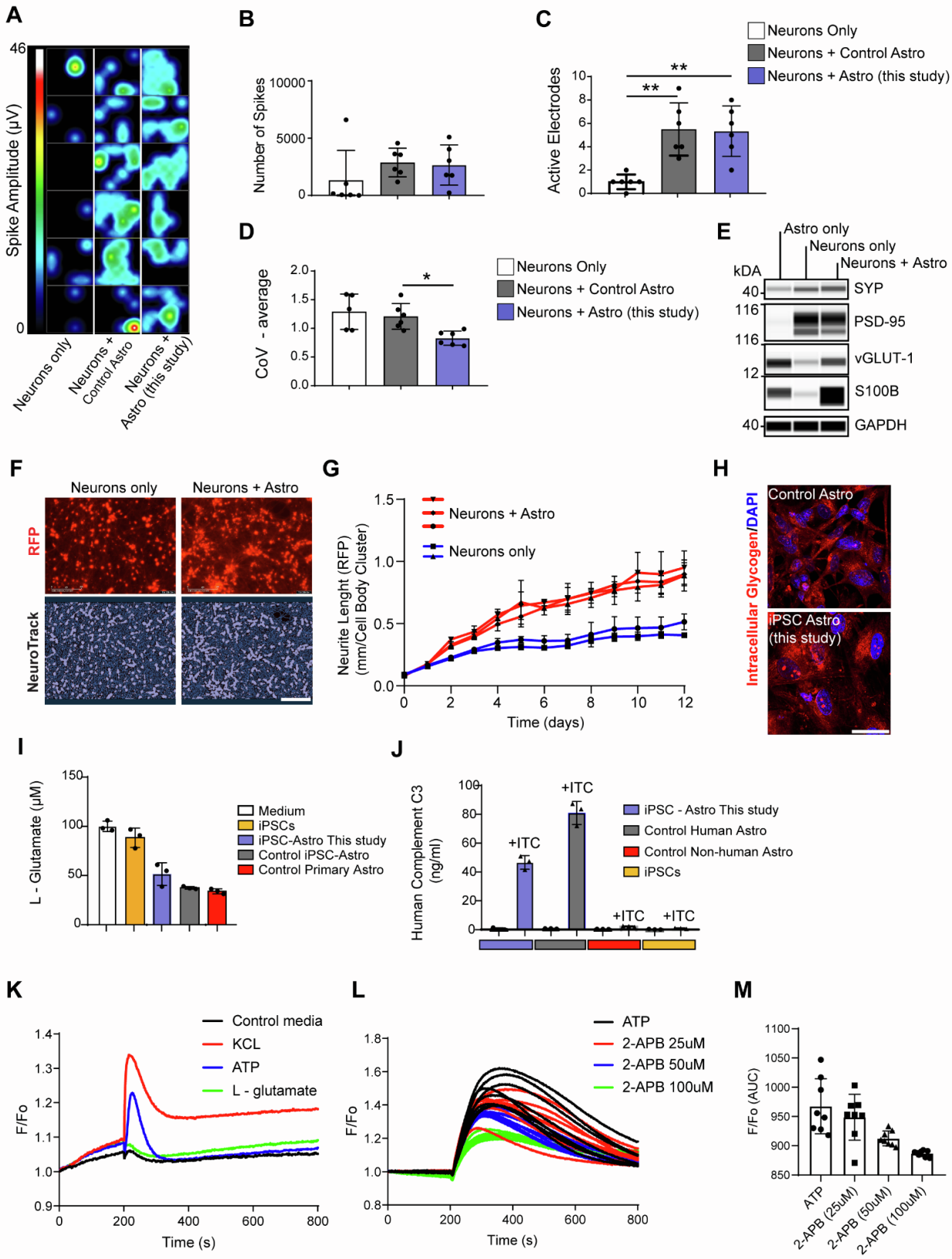
A
Spike Amplitude (µV)
46
0
Neurons only
Neurons + Control Astro
Neurons + Astro (this study)
B
Number of Spikes
10000
5000
0
C
Active Electrodes
Neurons Only
Neurons + Control Astro
Neurons + Astro (this study)
**
**
D
CoV - average
*
Neurons Only
Neurons + Control Astro
Neurons + Astro (this study)
E
Astro only
Neurons only
Neurons + Astro
kDA
SYP
PSD-95
vGLUT-1
S100B
GAPDH
F
Neurons only
Neurons + Astro
RFP
NeuroTrack
G
Neurite Lenght (RFP) (mm/Cell Body Cluster)
Neurons + Astro
Neurons only
Time (days)
H
Intracellular Glycogen/DAPI
Control Astro
iPSC Astro (this study)
I
L - Glutamate (µM)
Medium
iPSCs
iPSC-Astro This study
Control iPSC-Astro
Control Primary Astro
J
Human Complement C3 (ng/ml)
+ITC
iPSC - Astro This study
Control Human Astro
Control Non-human Astro
iPSCs
K
F/Fo
Control media
KCL
ATP
L - glutamate
Time (s)
L
F/Fo
ATP
2-APB 25uM
2-APB 50uM
2-APB 100uM
Time (s)
M
F/Fo (AUC)
ATP
2-APB (25uM)
2-APB (50uM)
2-APB (100uM)

Figure S3. Functional characterization of hPSC-derived astrocytes

(A) MEA analysis showing enhanced electrical activity of glutamatergic neurons co-cultured with hPSC-astrocytes for 8 days.

(B-D) Quantification of spikes (B), active electrodes (C) and reduced coefficient of variation (D) in co-cultures as compared to neuron-only cultures. n = 6 replicate wells per experimental condition. Glutamatergic neurons and control astrocytes (FUJIFILM CDI), iPSC-astrocytes derived with the current method (LiPSC GR 1.1).

(E) Western blot analysis of neuronal markers synaptophysin (SYP), PSD-95, vesicular glutamate transporter-1 (vGLUT1), and the astrocyte marker S100B in co-cultures (21 day). Note the stronger expression of SYN and S100B in co-cultures suggesting improved differentiation of both cell types.

(F) Representative images of RFP^+ i3-neurons and image mask of cell bodies and neurites analyzed with NeuroTrack software. Co-cultured astrocytes and i3-neurons derived from the same iPSC line (WTC11).

(G) Time-course live-cell imaging and quantification of RFP^+ neurite length in neuron-only versus neuron-astrocyte co-cultures. Note the difference from day 2 onward. i3-neurons were co-cultured with astrocytes in a 1:3 ratio. Images were obtained with the IncuCyte S3 live imaging system (each data point on the graph represents a replicate well; for each well 4 images were taken and analyzed over the course of 12 days; n = 3 replicate wells for co-cultures, n = 2 replicate wells for mono-cultures).

(H) PAS stain showing intracellular glycogen in hPSC-astrocytes (LiPSC-GR1.1) and controls (iCell Astrocytes from FUJIFILM CDI). Scale bar, 100 μm

(I) Glutamate uptake by iPSC-astrocytes (NCRM5) is comparable to controls (FUJIFILM CDI) and primary mouse astrocytes (ScienCell). n = 3 replicate wells.

(J) Human complement C3 secretion by iPSC-astrocytes (NCRM5) and controls into the culture medium after stimulation with inflammatory cytokines (IL-1b, TNF-alpha and C1q) for 24 h. n = 3 replicate wells.

(K) Calcium transients in iPSC-astrocyte cultures (LiPSC-GR1.1) after stimulation with KCL, ATP and L-glutamate. Each dotted line in the graph represents average from n = 6 replicate wells.

(L) Calcium transients in iPSC-astrocyte cultures (LiPSC-GR1.1) after stimulation with ATP, pretreated for 1h with DMSO (black lines) or IP3R antagonist 2-APB in dose response manner (25, 50 and 100 μM). Each dotted line in the graph represents one well.

(M) Quantification of the area under the curve (AUC) showing reduced calcium response after 2-APB pretreatment.

Figure S4

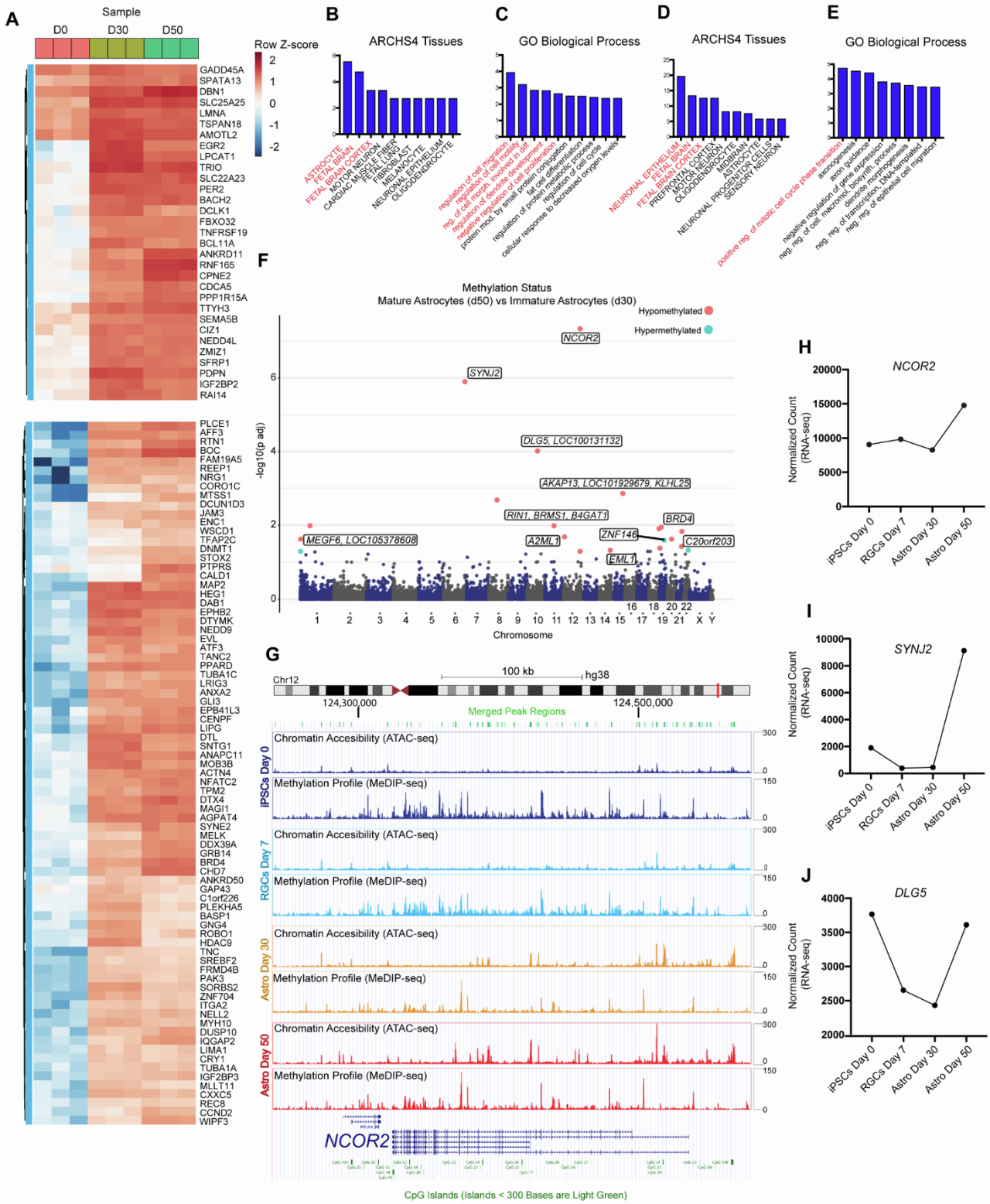
A
Sample
D0
D30
D50
Row Z-score
2
1
0
-1
-2
GADD45A
SPATA13
DBN1
SLC25A25
LMNA
TSPAN18
AMOTL2
EGR2
LPCAT1
TRIO
SLC22A23
PER2
BACH2
DCLK1
FBXO32
TNFRSF19
BCL11A
ANKRD11
RNF165
CPNE2
CDCA5
PPP1R15A
TTYH3
SEMA5B
CIZ1
NEDD4L
ZMIZ1
SFRP1
PDPN
IGF2BP2
RAI14
PLCE1
AFF3
RTN1
BOC
FAM19A5
REEP1
NRG1
CORO1C
MTSS1
DCUN1D3
JAM3
ENC1
WSCD1
TFAP2C
DNMT1
STOX2
PTPRS
CALD1
MAP2
HEG1
DAB1
EPHB2
DTYMK
NEDD9
EVL
ATF3
TANC2
PPARD
TUBA1C
LRIG3
ANXA2
GLI3
EPB41L3
CENPF
LIPG
DTL
SNTG1
ANAPC11
MOB3B
ACTN4
NFATC2
TPM2
DTX4
MAGI1
AGPAT4
SYNE2
MELK
DDX39A
GRB14
BRD4
CHD7
ANKRD50
GAP43
C1orf226
PLEKHA5
BASP1
GNG4
ROBO1
HDAC9
TNC
SREBF2
FRMD4B
PAK3
SORBS2
ZNF704
ITGA2
NELL2
MYH10
DUSP10
IQGAP2
LIMA1
CRY1
TUBA1A
IGF2BP3
MLLT11
CXXC5
REC8
CCND2
WIPF3
B
ARCHS4 Tissues
ASTROCYTE
FETAL BRAIN
FETAL BRAIN CORTEX
MOTOR NEURON
CARDIAC MUSCLE FIBER
FETAL LUNG
FIBROBLAST
MELANOCYTE
NEURONAL EPITHELIUM
OLIGODENDROCYTE
C
GO Biological Process
regulation of cell migration
regulation of cell motility
reg. of cell motility involved in chemotaxis
regulation of dendrite development
negative regulation of cell proliferation
protein mod. by small protein conjugation
fat cell differentiation
regulation of protein metabolic process
regulation of cell cycle
cellular response to decreased oxygen levels
D
ARCHS4 Tissues
NEURONAL EPITHELIUM
FETAL BRAIN
FETAL BRAIN CORTEX
PREFRONTAL CORTEX
MOTOR NEURON
OLIGODENDROCYTE
MIDBRAIN
ASTROCYTE
NEURONAL PROGENITOR CELLS
SENSORY NEURON
E
GO Biological Process
positive reg. of mitotic cell cycle phase transition
axonogenesis
axon guidance
negative regulation of gene expression
neg. reg. of cell. macromol. biosynth. process
dendrite morphogenesis
neg. reg. of transcription, DNA-templated
neg. reg. of epithelial cell migration
F
Methylation Status
Mature Astrocytes (d50) vs Immature Astrocytes (d30)
Hypomethylated
Hypermethylated
NCOR2
SYNJ2
DLG5, LOC100131132
AKAP13, LOC101929679, KLHL25
RIN1, BRMS1, B4GAT1
BRD4
MEGF6, LOC105378608
A2ML1
ZNF146
C20orf203
EML1
-log10(p adj)
Chromosome
G
Chr12
100 kb
hg38
124,300,000
124,500,000
Merged Peak Regions
iPSCs Day 0
RGCs Day 7
Astro Day 30
Astro Day 50
Chromatin Accesibility (ATAC-seq)
Methylation Profile (MeDIP-seq)
NCOR2
CpG Islands (Islands < 300 Bases are Light Green)
H
NCOR2
Normalized Count (RNA-seq)
iPSCs Day 0
RGCs Day 7
Astro Day 30
Astro Day 50
I
SYNJ2
J
DLG5

Figure S4. Epigenetic changes during directed gliogenic differentiation

(A) Chromatin accessibility in hPSCs (day 0) and astrocytes (day 30, 50) considering the top 300 genes expressed by fetal and adult astrocytes (Zhang et al., 2016). Heatmaps show genes with strongest difference for chromatin accessibility. Dynamic chromatin changes identify two dominant gene clusters with open chromatin (upper panel showing 31 genes, lower panel showing 79 genes).

(B-E**)** Enrichr analysis of identified genes (*GO Biological process* and *ARCHS4 Tissues*).

(F) Manhattan plot displaying differential gene methylation with strongest difference between immature $GFAP^-$ (day 30) and mature astrocytes $GFAP^+$ (day 50). *NCOR2* hypomethylation in mature astrocytes (day 50) is the most significant hit when compared to immature astrocytes at day 30.

(G) UCSC Genome Browser plots showing chromatin accessibility and methylation profile of *NCOR2* gene loci across differentiation time-points. Note that *NCOR2* is hypermethylated in iPSC (Day 0) and RGCs (Day 7) and hypomethylation and open chromatin is detectable in astrocytes (day 30 and 50).

(H-J) Time-course transcriptomics (RNA-seq) showing strong expression of *NCOR2, SYNJ2* and *DLG5* by day 50. n = 3 independent astrocyte differentiation experiments (NCRM5).

Figure S5

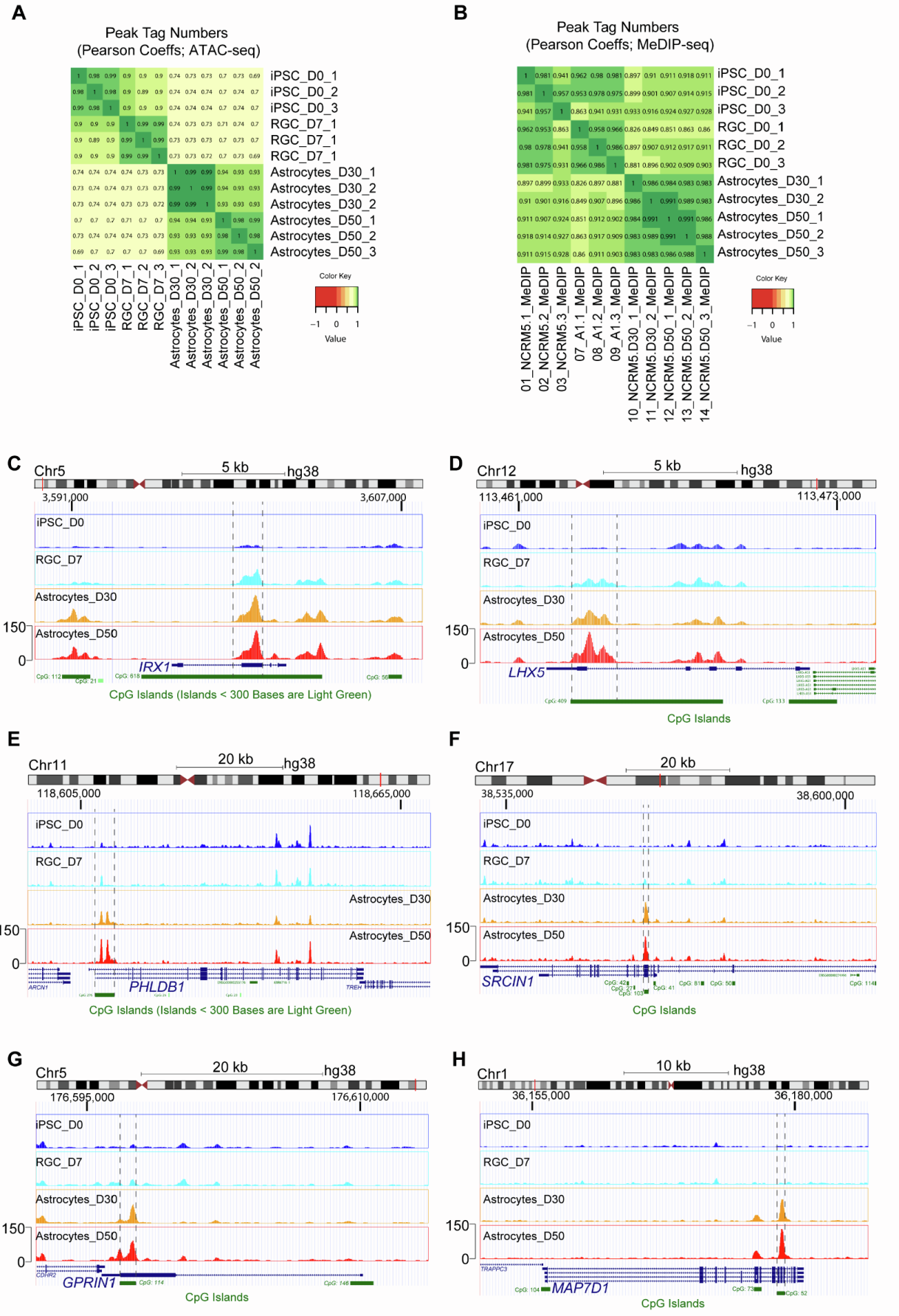
A
Peak Tag Numbers
(Pearson Coeffs; ATAC-seq)
iPSC_D0_1
iPSC_D0_2
iPSC_D0_3
RGC_D7_1
RGC_D7_2
RGC_D7_3
Astrocytes_D30_1
Astrocytes_D30_2
Astrocytes_D30_2
Astrocytes_D50_1
Astrocytes_D50_2
Astrocytes_D50_2
Color Key
Value
B
Peak Tag Numbers
(Pearson Coeffs; MeDIP-seq)
iPSC_D0_1
iPSC_D0_2
iPSC_D0_3
RGC_D0_1
RGC_D0_2
RGC_D0_3
Astrocytes_D30_1
Astrocytes_D30_2
Astrocytes_D50_1
Astrocytes_D50_2
Astrocytes_D50_3
01_NCRM5.1_MeDIP
02_NCRM5.2_MeDIP
03_NCRM5.3_MeDIP
07_A1.1_MeDIP
08_A1.2_MeDIP
09_A1.3_MeDIP
10_NCRM5.D30_1_MeDIP
11_NCRM5.D30_2_MeDIP
12_NCRM5.D50_1_MeDIP
13_NCRM5.D50_2_MeDIP
14_NCRM5.D50_3_MeDIP
Color Key
Value
C
Chr5
5 kb
hg38
3,591,000
3,607,000
iPSC_D0
RGC_D7
Astrocytes_D30
Astrocytes_D50
150
0
IRX1
CpG Islands (Islands < 300 Bases are Light Green)
D
Chr12
5 kb
hg38
113,461,000
113,473,000
iPSC_D0
RGC_D7
Astrocytes_D30
Astrocytes_D50
150
0
LHX5
CpG Islands
E
Chr11
20 kb
hg38
118,605,000
118,665,000
iPSC_D0
RGC_D7
Astrocytes_D30
Astrocytes_D50
150
0
PHLDB1
CpG Islands (Islands < 300 Bases are Light Green)
F
Chr17
20 kb
38,535,000
38,600,000
iPSC_D0
RGC_D7
Astrocytes_D30
Astrocytes_D50
150
0
SRCIN1
CpG Islands
G
Chr5
20 kb
hg38
176,595,000
176,610,000
iPSC_D0
RGC_D7
Astrocytes_D30
Astrocytes_D50
150
0
GPRIN1
CpG Islands
H
Chr1
10 kb
hg38
36,155,000
36,180,000
iPSC_D0
RGC_D7
Astrocytes_D30
Astrocytes_D50
150
0
MAP7D1
CpG Islands

Figure S5. Methylation signature of differentiated astrocytes.

(A,B) Correlation heatmaps showing Pearson coefficients of all pairwise comparisons, colored from dark green (high correlation) to yellow and red (low or no correlation). Lower correlation in chromatin accessibility across differentiation suggests more dynamic chromatin changes (A) relative to DNA methylation changes (B).

(C-H) UCSC Genome Browser plots showing gene loci hypermethylated in iPSC-astrocytes. Peaks marked by the dotted line are within the CpG island regions of (C) *IRX1*, (D) *LHX5*, (E) *PHLDB1*, (F) *SRCIN1*, (G) *GPRIN1* and (H) *MAP7D1*. n = 3 independent astrocyte differentiation experiments (NCRM5).

Figure S6

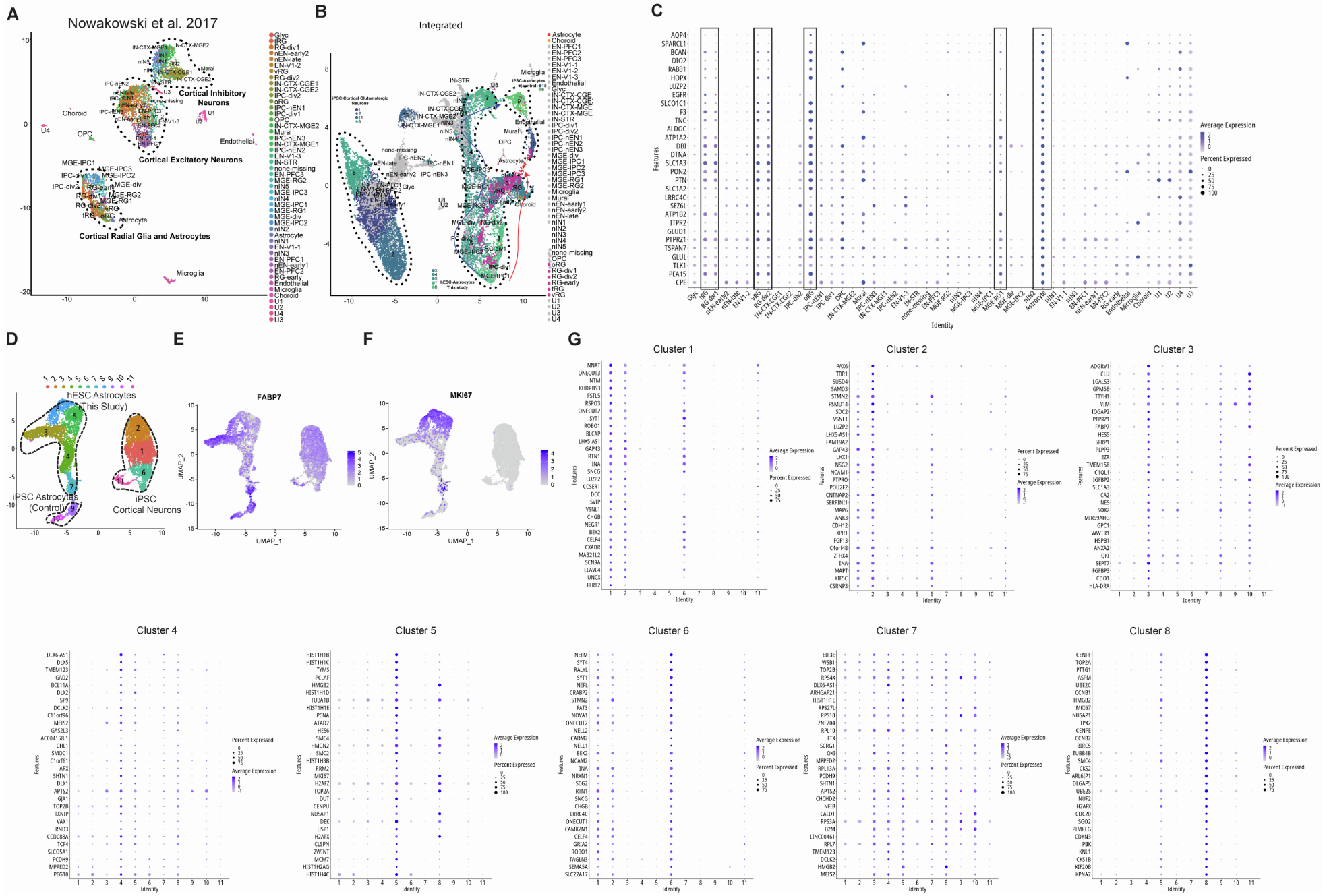
A
Nowakowski et al. 2017
Cortical Inhibitory Neurons
Cortical Excitatory Neurons
Cortical Radial Glia and Astrocytes
B
Integrated
C
Identity
Average Expression
Percent Expressed
D
hESC Astrocytes (This Study)
iPSC Astrocytes (Control)
iPSC Cortical Neurons
E
FABP7
F
MKI67
G
Cluster 1
Cluster 2
Cluster 3
Cluster 4
Cluster 5
Cluster 6
Cluster 7
Cluster 8

Figure S6. Integrated single-cell transcriptomic analysis of hPSC-astrocytes and comparison to human fetal cortex

(A) UMAP representation of 4,261 cells from the Nowakowski et al. study sampled across the human cortex development (gestational week 5 – 37) outlines three broad clusters excitatory neurons, inhibitory neurons, and radial glia/astrocyte.

(B) UMAP showing the integration of hPSC-derived astrocytes and cortical excitatory neurons with a published dataset (Nowakowski et al., 2017). Due to the differences in the number of profiled cells hPSC-cluster sizes were significantly larger. Note that hPSC-derived astrocytes cluster together with radial glia and astrocytes.

(C) Feature plot depicting the top 30 genes expressed in human fetal astrocyte cluster and high similarity to radial glia clusters (boxed) (adopted from Nowakowski et al., 2017).

(D) UMAP representation of unbiased clustering of hPSC-astrocyte samples. Seurat analysis identified 8 different clusters.

(E-F) Feature plots demonstrating *FABP7* and *MKI67* expression across astrocyte clusters.

(D) Dot plots showing the top 30 gene features for each of the astrocyte clusters.

Data from 4261 single cells (Nowakowski et al., 2017) was used for data integration. Data from 6138 single cells from derived astrocytes (WA09) and 744 control astrocytes (FUJIFILM CDI). Single-cell RNA-seq data were analyzed in the Seurat R package.

Figure S7

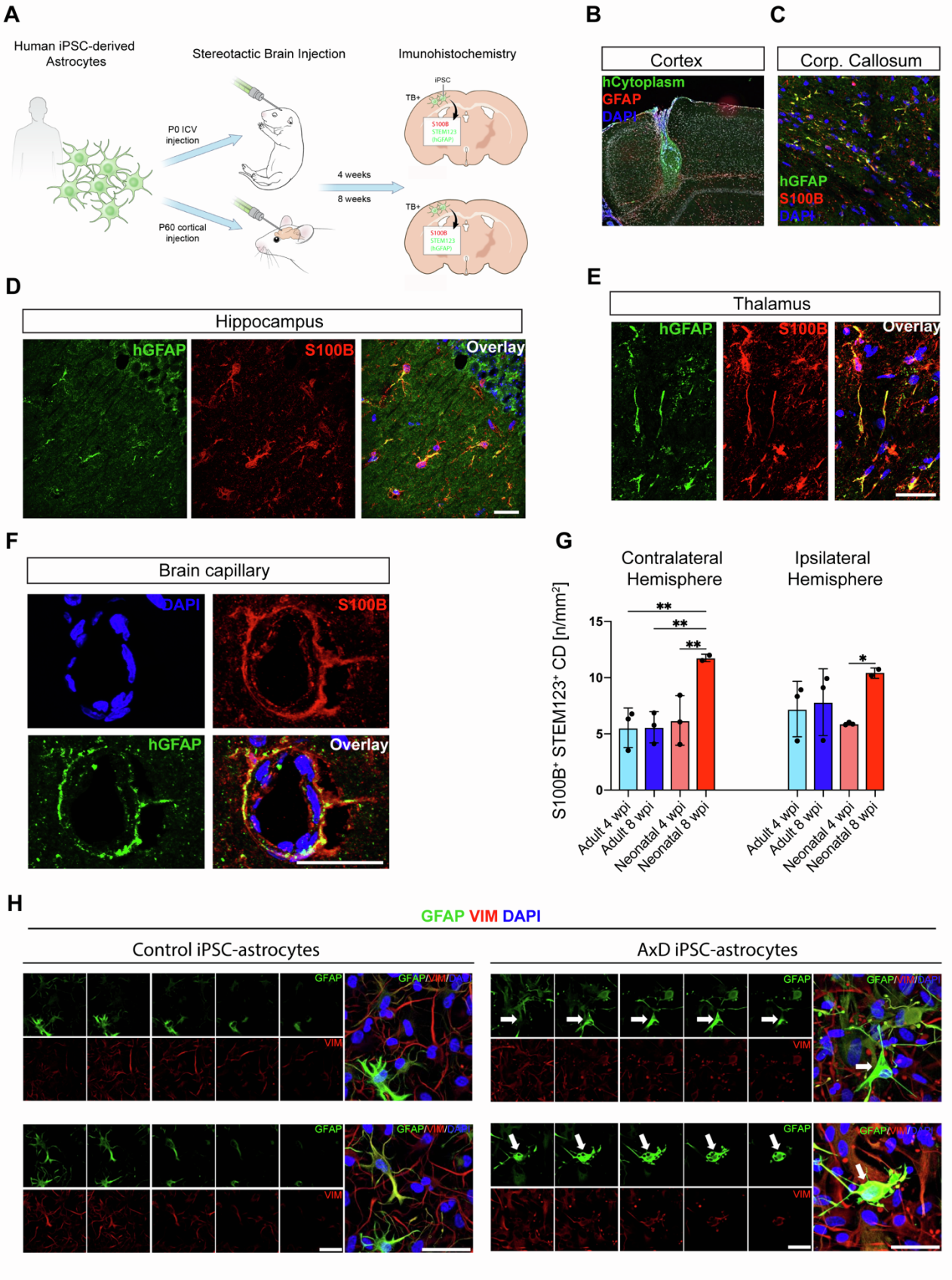
A
Human iPSC-derived Astrocytes
Stereotactic Brain Injection
Imunohistochemistry
P0 ICV injection
P60 cortical injection
4 weeks
8 weeks
iPSC
TB+
S100B
STEM123
(hGFAP)
B
Cortex
hCytoplasm
GFAP
DAPI
C
Corp. Callosum
hGFAP
S100B
DAPI
D
Hippocampus
hGFAP
S100B
Overlay
E
Thalamus
hGFAP
S100B
Overlay
F
Brain capillary
DAPI
S100B
hGFAP
Overlay
G
Contralateral Hemisphere
Ipsilateral Hemisphere
S100B+ STEM123+ CD [n/mm2]
15
10
5
0
**
**
**
*
Adult 4 wpi
Adult 8 wpi
Neonatal 4 wpi
Neonatal 8 wpi
H
GFAP VIM DAPI
Control iPSC-astrocytes
AxD iPSC-astrocytes
GFAP
VIM
GFAP/VIM/DAPI

Figure S7. Brain engraftment of human astrocytes and analysis of iPSC-derived astrocytes from AxD patient

(A) Schematic of experimental design and treatment groups.

(B) Human iPSC-astrocytes (NCRM5) transplanted into the adult mouse cortex (4 weeks post-grafting) show strong immunoreactivity against human cytoplasmic marker STEM121 and GFAP.

(C) Immunostaining for human-specific GFAP (STEM123 antibody) and S100B detect migratory cells in the corpus callosum.

(D-E) Immunostaining for human specific GFAP (STEM123) showing cells in the thalamus and hippocampus indicating long-distance migration of astrocytes grafted into the cortex.

(F) Human GFAP-expressing astrocytes surrounding a blood vessel in the mouse brain parenchyma.

(G) Quantification of $S100B^+$ and $hGFAP^+$ co-labeled cells in the ipsi- and contralateral hemispheres of adult and neonatal mice at 4- and 8-weeks post-grafting (n = 3 animals per group).

(H) Confocal images (1 μm optical sections) showing $GFAP^+$ aggregates and aberrant astrocyte morphology in AxD astrocytes (GM16825) but not control astrocytes (NCRM5).

Scale bars (B-F) 100 μm, (H) 50 μm.

Movie S1. Slow spontaneous calcium transients in astrocytes

Video-microscopy of iPSC-derived astrocytes (day 50, LiPSC GR1.1) loaded with calcium dye (FLIPR Calcium 6 kit). Note the spreading of calcium transients across the cell culture.

Movie S2. Slow spontaneous calcium transients in control astrocytes

Video-microscopy of iCell astrocytes (FUJIFILM CDI) loaded with calcium dye (FLIPR Calcium 6 kit). Note that these control astrocytes behave similarly to the iPSC-derived astrocytes shown in Movie S1.

Supplementary Table 1

Protein densitometry values associated with Figures S2 and S3.

Experimental Procedures

Differentiation of hPSCs into RGCs and astrocytes

For RGC differentiation, hPSCs were detached using 0.5 mM EDTA and plated at 10.000 cell/cm^2 density on a VN-coated surface in E8 medium supplemented with CEPT (day -1). The following day medium was replaced with freshly prepared Astro-1. On day 3, cells were dissociated using 0.5 mM EDTA and 20.000 cell/cm^2 were plated on a VN-coated surface in Astro-1 medium supplemented with CEPT for 24 h. Daily Astro-1 medium changes were performed to generate neural rosettes by day 7. For patterning RGCs into OTX2$^+$ neural progenitors, 0.8 μM CHR99021 (Tocris, 4423) + 100 ng/mL FGF8b (R&D Systems, 423-F8) were added to Astro-1 medium between days 7-15. For patterning RGCs into HOXA2$^+$ progenitors, 1 μM CHR99021 (Tocris, 4423) was added to Astro-1 medium between days 7-15.

For astrocyte differentiation, RGCs were maintained in Astro-1 medium until day 15, with daily medium changes. Cell passaging was performed on days 7, 11, and 14 using Accutase and at each passaging step 30,000 cells/cm^2 were plated on VN-coated plates in Astro-1 medium supplemented with CEPT for 24 h. On day 15, medium was replaced by Astro-2. Medium changes were performed daily with passaging on day 18 and 23, and 40.000 cells/cm^2 were plated on VN-coated plates and maintained until day 30. On day 30, cells were either cryopreserved in Astro-2 medium supplemented with 10% DMSO and CEPT or further matured in Astro-3 medium until day 50.

For astrocyte maturation, day-30 astrocytes were plated on Geltrex (Thermo Fisher Scientific, A1569601) at 50.000 cells/cm^2 and maintained in Astro-3 medium until day 50. Astro-3 medium was based on DMEM/F12 medium supplemented with N2, B27 with vitamin A, 1% lipid supplement (Gibco) and JAGGED-1, DLL-1, LIF, CNTF all at 10 ng/ml concentration, hNRG1/EGF domain 20 ng/ml, 2 μM forskolin, 200 nM phorbol-ester, 40 ng/ml triiodothyronine and 200 μM ascorbic acid. Cultures were passaged (1:2 ratio) on day 37 and 43, respectively. On day 50, cells were cryopreserved in Astro-3 medium supplemented with 10% DMSO and CEPT.

For robotic astrocyte differentiation, 1.75 million hPSCs were plated in T175 flasks and cultured in the CompacT SelecT system (Sartorius) and Astro-1, Astro-2, and Astro-3 media were applied as described above. All media

changes (Days 0-50) were performed by the robotic instrument throughout the cell differentiation process. Cell culture flasks were only briefly removed from the system for offline centrifugation to remove Accutase that was used for cell dissociation.

Differentiation with Astro-1/Astro-2 versus alternative media

To generate NFIA$^+$ RGCs, cells were treated for 7 days in Astro-1 and 7 days in Astro-2, or the same basal medium (DMEM/F12; N2; B27 without vit. A) supplemented with 25 ng/ml EGF (R&D systems, 236-EG), 25 ng/ml FGF2 (R&D systems, 3718-FB) and 2% FBS (Gibco, A4766801) and 10 ng/ml LIF. Cells were passaged on days 11, 14 and 18 and plated at 30.000, 40.000 and 40.000 cells/cm^2. At day 21, cells were washed in PBS, harvested using a cell scraper and cell pellets frozen on dry ice after centrifugation and removal of PBS (Figure 2A and 2B).

To compare NFIA induction across 6 treatment combinations (Figure S3), three independent hPSC lines (WA09 hESC, NCRM5 and LiPSC GR1.1) were treated as follows:

i. BMP inhibitor LDN193189 (100nM) from day 0-14 followed by Astro-2 (day 14-21);

ii. LDN193189 (100nM) and TGFß inhibitor A83-01 (2 μM) for the first 7 days, followed by EGF/FGF2 (25 ng/ml each), day 7- 21.

iii. Astro-1/Astro-2 combination following the described protocol.

iv. Astro-1 supplemented with EGF/FGF2 (25 ng/ml each)/Astro-2 supplemented with EGF/FGF2 (25 ng/ml each); v. Astro-1/Astro2 supplemented with EGFR inhibitor Afatinib (1 μM) and FGFR 1/2/3 inhibitor PD173074 (25 nM).

vi. Astro-1 with removal of NOTCH ligands (DLL-1 and Jagged-1)/ Astro-2 with removal of NOTCH ligands (DLL-1 and Jagged-1).

Importantly, the same basal media components and passaging timepoints, and other experimental steps were performed across all conditions. At day 21, cells were washed in PBS, and harvested using a cell scraper and cell pellets frozen on dry ice after centrifugation and removal of PBS.

Immunocytochemistry

Cells cultured in 6-, 24- or 96-well plates or 8 chamber slides (Ibidi) were fixed with 4% PFA diluted in PBS for 15 min and washed 3 times with PBS (5 min each). Blocking was performed with 4% donkey serum and 0.1% Triton-X in PBS for 1h at room temperature on a shaker. All primary antibodies in this study were applied overnight at 4°C. Next day, cultures were washed 3 times with PBS and appropriate secondary antibodies were applied for 1h at room temperature. Fluorescence images were taken with the Leica DMi8 epifluorescence and Zeiss LSM 710 confocal microscopes using appropriate filters. Primary antibodies used for immunocytochemistry are as follows: mouse anti-PAX6 1:200 (BD Biosciences, 561462,), rabbit anti-FABP7 (BLBP) 1:200 (EMD Millipore, ABN14), rabbit anti-CD44 1:400 (Abcam, ab157107), rat anti-CD44 1:100 (Abcam, A25528), mouse anti-VIMENTIN 1:500 (DAKO, M0725), rabbit anti-NFIA 1:250 (Novus, NBP-1-81406), rabbit anti-S100-beta 1:100 (Abcam, ab52642), mouse anti-TUJ1 1:1000 (BioLegend, 801201), rabbit anti-GFAP 1:1000 (DAKO, Z0334), rabbit anti-SYNAPSIN-1 1:500 (Synaptic Systems, 106-011), rabbit anti-ASPM 1:100 (Novus, NB-100-2278), rabbit anti-FAT1 1:100 (Millipore-Sigma, HPA023882) and mouse anti-Pan-Neuronal Marker (PNM) 1:200 (EMD Millipore, MAB2300), goat anti-OTX2 1:50 (R&D systems, AF1979), rabbit anti-HOXA2 1:200 (Sigma Aldrich, HPA078220), OLIG2 (Millipore Sigma, AB9610) . The following secondary antibodies were used: donkey anti-mouse Alexa 568 (1:500, A-10037, Thermo Fisher Scientific) and donkey anti-rabbit Alexa Fluor 488 (1:500; A-21206, Thermo Fisher Scientific).

Western blot

The Wes and Jes automated Western blotting systems (Protein Simple) were used for quantitative analysis of protein expression as described previously(Chen et al., 2021; Tristan et al., 2020; Tristan et al., 2021). Western blots are displayed by lanes in virtual blot-like images. Briefly, cells were harvested by scraping, pelleted, washed with PBS, flash frozen using dry ice and stored at -20 °C until processed. Cell pellets were resuspended in RIPA buffer (Thermo Fisher Scientific) supplemented with halt protease inhibitor cocktail (Thermo Fisher Scientific) and lysed by sonication. Lysates were cleared of debris by centrifugation at 14,000 g for 15 min and quantified using the BCA protein assay kit (Thermo Fisher Scientific). Lysates were diluted 1:4 with 1X sample buffer (Protein Simple). Protein quantification was performed using the 12-230 kDa 13 25-lane plate (PS-MK15; Protein

Simple) in a Wes Capillary Western Blot analyzer according to the manufacturer's recommendation. Protein quantification was done using the Compass software. Primary antibodies used are as follows: mouse anti-GAPDH 1:2,000 (Santa Cruz, sc25778,), rabbit anti-PAX6 1:20 (BioLegend, 901301), rabbit anti-FAT1 1:20 (MilliporeSigma, HPA023882), rabbit anti-ATF4 1:50 (Cell Signaling Technology, D4B8), rabbit anti LC3 A/B 1:50 (Cell Signaling Technology, D3U4C), rabbit anti-ATG3 1:50 (Cell Signaling Technology, 3415), rabbit anti-ATG5 1:50 (Cell Signaling Technology, D5F5U), rabbit anti-TDP43 total 1:50 (Cell Signaling Technology, 89789) and rabbit anti-phospho-TDP43 1:50 (Thermo Fisher Scientific, 22309-1-AP), mouse anti-TUBB3 (TUJ1) 1:50 (BioLegend, MMS-435P), rabbit anti-CD133 1:50 (Abcam, ab19898), rabbit anti-S100-beta 1:50 (Abcam, ab52642), mouse anti-Synaptophysin-1 1:50 (Synaptic Systems, 101 011), rabbit anti phospho-AKT (Cell Signaling Technology, 4060S), rabbit anti phospho-p44/42 MAPK (Cell Signaling Technology, 4376S), rabbit anti AKT (Cell Signaling Technology, 9272), rabbit anti p44/42 MAPK (Cell Signaling Technology, 4695), rabbit anti EGFR (Cell Signaling Technology, 4267).

Transmission Electron Microscopy (TEM)

Astrocytes differentiated from hPSC (day 30 and 50) and cultured in 6-well plates (1 million cells per well) and control astrocytes (FUJIFILM CDI, 01434) were fixed by replacing the media with 2.5% glutaraldehyde in PBS (pH 7.2–7.4) for 60 minutes at room temperature. Sample processing for electron microscopy and imaging (Hitachi, H7659) was performed by the Electron Microscopy Laboratory of Leidos Biomedical Research, NCI, Frederick, MD.

RNA Scope Fluorescent Multiplex Assay

One day before fixation (day 6), Astro-1 or dSMADi treatment cells were seeded on 4-chamber slides (Ibidi) coated with VN in Astro-1 medium or dSMADi at a high-density that allowed cells to be 80–90% confluent at the time of fixation. After removal of growth medium, cells were briefly washed with PBS and fixed in 10% PFA for 30 mins. Following fixation, cells were rinsed twice in PBS before dehydration by submerging in a series of ethanol solutions (50%, 70% and 100%). Rehydrated cells were pretreated to block endogenous peroxidase activity and optimally permeabilize samples to allow probe access to target RNA using pretreatment kit (ACD,

322380). The hybridization was performed according to RNAscope® Fluorescent Multiplex Kit protocol (ACD, 320293) using custom made RNAscope® Probe- Hs-BIRC5 (ACD, 465361) and positive control RNAscope® Positive Control Probe- Hs-POLR2A (ACD,310451). Fluorescence images were taken with the Leica DMi8 epifluorescence microscope.

Co-culturing astrocytes and neurons

For co-culture experiments, iPSC-derived glutamatergic or motor neurons (FUJIFILM CDI, R1061, R1051) were plated on Geltrex-coated plates (100,000 cells per cm^2) and placed into the incubator (37 °C) for 45 mins to allow cell attachment. Then, 33,000 astrocytes were added per cm^2 to achieve a 1:3 ratio. The neuronal medium recommended by the vendor (FUJIFILM CDI) was supplemented with 10 ng/ml LIF (R&D Systems), 10 ng/ml CNTF (R&D Systems) and 1% lipid supplement (Gibco). CEPT was included for the first 24 h. Co-cultures were maintained for up to 21 days prior to fixation with 4% PFA and immunostaining. Control astrocytes (FUJIFILM CDI, 01434) are >95% pure cultures with the expression of typical markers (e.g., S100β and GFAP).

Brain spheroids and oligodendrocyte precursor differentiation from RGCs

Cortical spheroids were cultured based on a published method (Marton et al., 2019) with the exception that spheroid formation was initiated using RGCs. Briefly, RGCs (WA09) were dissociated at day 7 using Accutase (Thermo Fisher Scientific) and plated in 96-well ultra-low attachment (ULA) round-bottom plates (Corning) at a density of 20,000 cells per well in expansion media consisted of DMEM/F12-Glutamax(Gibco) media with 1% N2 supplement (Gibco), 2% B27 without vitamin A (Gibco), 20 ng/mL human EGF (R&D) and 20 ng/mL human FGF (R&D). The cells were treated with the CEPT cocktail (Chen et al., 2021) for the first 24 h, followed by media change with expansion media. At day 3, the aggregated cells were transferred to ULA 24-well plates (Corning) at density of 1 sphere/well with 500 μl of expansion media. The medium was changed every other day. At day 7, the medium was changed to maturation medium which was consisted of DMEM/F12-Glutamax (Gibco) with 1% N2 supplement (Gibco), 2% B27 (Gibco), 25 ng/mL human BDGF (R&D), 25 ng/mL human GDNF (R&D), 25 ng/mL human NT-3 (R&D), 200 μM ascorbic acid (Tocris), and 1mM dbCAMP (Tocris). All cultures were maintained at 37 °C under humidified 5% CO_2 and atmospheric oxygen. Organoids were fixed in 4% PFA at

room temperature for 20 min, washed with PBS three times, and incubated in 30% sucrose at 4°C overnight. Tissues were embedded in O.C.T. compound (Fisher Scientific), cut into 10-μm sections, and mounted on microscope slides. For immunohistochemical analysis, sections were permeabilized and blocked with 0.3% Triton X-100 and 5% BSA in PBS for 1h. Slides were mounted with ProLong Glass Antifade Mountant with NucBlue Stain (Thermo Fisher Scientific). Fluorescence images were taken with the Zeiss LSM 710 confocal microscope using appropriate filters.

For oligodendrocyte precursor cell differentiation in monolayer cultures, hPSC-derived RGCs (WA09; LiPSC GR 1.1) were differentiated for 21 days, with passaging every 4-5 days (30.000 cell/cm^2), using SAG21k (0.5 μM), EGF/FGF2 (25 ng/ml each) and RA (1 μM) added to Astro-1 medium. After 3 weeks (passage 5) immunocytochemistry was performed for OLIG2 expression.

Multi-electrode array

Electrophysiology was performed using the Maestro platform (Axion Biosystems). Glutamatergic neurons (FUJIFILM CDI, R1062) were plated at a density of ~5 million neurons per cm^2 in complete neuronal media as recommended by the vendor: BrainPhys Neuronal Medium (STEMCELL Technologies, 05790) supplemented with iCell Neural Supplement B (FUJIFILM CDI, M1029) and iCell Nervous System Supplement (FUJIFILM CDI, M1031), N2 (Gibco), 10 µg/mL laminin (Thermo Fisher Scientific), 10 ng/ml LIF (R&D Systems), 10 ng/ml CNTF (R&D Systems) and 1% lipid supplement (Gibco) and CEPT. 48-well plates with electrodes were coated with 0.1% polyethylenimine (PEI). Motor neurons (FUJIFILM CDI) were plated at a density of ~5 million neurons per cm^2 in complete medium containing CEPT. For co-culture experiments with neurons, iPSC-astrocytes generated at NCATS were compared to control iCell Astrocytes (FUJIFILM CDI, R1092). Plating of astrocytes and neurons in 1:3 ratio is described above. 48-well MEA plates were coated with Geltrex (Gibco). Twenty-four hours post-plating, fresh medium was added and CEPT was removed and then 50% media changes were performed every 2-3 days. Electrophysiological recordings were performed daily for 10 min.

High-throughput calcium imaging

hPSC-derived astrocytes were plated onto Geltrex-coated 96-well plates with transparent bottom (Greiner) and maintained in Astro-3 media for 5-7 days with daily media changes prior to calcium imaging. Calcium imaging was performed on the FLIPR Penta high-content calcium imager (Molecular Devices). On the day of the experiment, cultures were prepared according to the instructions detailed in the FLIPR Calcium Assay 6 kit (Molecular Devices). Briefly, cells were loaded using 100 µl of prepared loading buffer without removing media portion (100 µl) and incubated for 2 h at 37 °C. After incubation, the 96 well cell plate was transferred to the FLIPR instrument and the experiment was initiated by taking 200 measurements of basal signal levels followed by administration of DMSO, L-glutamate (100 µM), ATP (30 µM) or KCl (65 mM), and recording of 600 measurements (read interval 1/s). For IP3R profiling experiments, 1h pretreatment with different dosages of 2-APB (Tocris, 1244) was performed during the second hour of incubation with the loading buffer.

Glutamate uptake assay

hPSC-derived astrocytes, control astrocytes (FUJIFILM CDI), mouse astrocytes (ScienCell) and hPSCs (negative control) were plated onto Geltrex-coated 96-well plates (Corning) and maintained in Astro-3 medium (astrocytes) or E8 medium (hPSCs) for 5-7 days with daily media changes prior to performing glutamate uptake assay. On the day of the experiment, cells were first incubated for 30 min in Hank's balanced salt solution (HBSS) buffer without calcium and magnesium (Gibco), prior to 3 h incubation with 100 µM L-glutamate in HBSS with calcium and magnesium (Gibco) to allow glutamate uptake by cells. After 3 h, medium/supernatant was analyzed with a colorimetric glutamate assay kit (Sigma-Aldrich, MAK004) according to the manufacturer's instructions.

Cytokine stimulation of astrocytes

hPSC-derived astrocytes, control astrocytes (FUJIFILM CDI), mouse astrocytes (ScienCell) and hPSCs were plated onto Geltrex coated 96 well plates (Corning) and maintained in Astro-3 medium (astrocytes) or E8 medium (hPSCs) for 5 – 7 days with daily medium changes prior to performing cytokine stimulation. On the day of the experiment, cells were treated with 3 ng/ml IL-1α (MilliporeSigma, SRP3310), 30 ng/ml tumor necrosis factor (Cell Signaling Technology, 8902SF) and 400 ng/ml C1q (MyBioSource, MBS143105) for 24 h. The

following day, medium was isolated, spun down to remove debris, and human complement C3 levels were measured using the Human Complement C3 ELISA Kit (Abcam, ab108823) following the manufacturer's instructions.

Live-cell metabolic assays using the Seahorse XF analyzer

The oxygen consumption rate (OCR) and extracellular acidification rate (ECAR) were analyzed using a Seahorse XF-96 analyzer (Agilent) according to the manufacturer's protocol. iPSC-astrocytes from Alexander disease (GM16825) and control astrocytes (NCRM5) were maintained in Astro-3 medium or Astro-3 medium supplemented with 3 ng/ml IL-1α (MilliporeSigma, SRP3310), 30 ng/ml tumor necrosis factor (Cell Signaling Technology, 8902SF) and 400 ng/ml C1q (MyBioSource, MBS143105) for 24 h prior to experiment. OCR and ECAR values were normalized to total cells per well.

High-content imaging and image analysis

hPSC (WA09, LiPSC GR 1.1, NCRM5) were seeded at 20.000 cells/cm2 in E8 with CEPT (day -1) and differentiated in the presence of Astro-1 or dSMADi (100 nM LDN-193189 + 2 μM SB431542) for 7 days in 6 well plates. For each cell line, 3 replicate wells were included in the experiment. On day 3, cells were dissociated (0.5 mM EDTA) and 20.000 cell/cm^2 was plated on VN-coated surface in Astro-1 medium supplemented with CEPT. Daily medium changes were performed using Astro-1 or dSMADi medium and cells were fixed in 4% PFA on day 7. After immunocytochemistry was performed against ZO-1 and FABP7, the central area of each well was imaged using Opera Phenix (PerkinElmer) high-content confocal imager (10x magnification). Images were imported from Opera Phenix to Columbus image analysis system (Perkin Elmer) and batch analysis was performed after ROI mask parameters were defined. Rosette lumen morphology was subjectively observed/identified as a connected image region, which was the size of multiple cells, where there was minimal DAPI staining and high relative levels of ZO-1 staining. The steps of the customized automated algorithm, which operates within the PerkinElmer Columbus high-content analysis platform, performed the following functions: 1) image filtering to enhance the local cluster pattern of ZO-1 staining, 2) blob detection [commercial proprietary algorithm, PerkinElmer] based on the enhanced ZO-1 image, 3) measurement of DAPI intensity and ZO-1

staining intensity within each blob region, 4) selection of blob regions as 'rosette lumen ROI masks' by thresholding DAPI intensity value and ZO-1 staining intensity value. DAPI and ZO-1 intensity thresholds were set empirically during assay development, and the same threshold values were applied to generate all batch analysis results.

Glycogen staining (Periodic Acid-Schiff)

hPSC-derived astrocytes and control astrocytes (FUJIFILM CDI) were washed with ice-cold PBS and fixed with ice-cold methanol for 5 min. After fixation, the Periodic Acid-Schiff staining kit (MilliporeSigma, 101646) was used according to manufacturer. Autofluorescence emitted by PAS-labeled granules was captured by using the Leica DMi8 epifluorescence microscope at 568 nm wavelength.

Cell transplantation

Adult male and female C57Bl/6J mice were purchased from The Jackson Laboratory (Maine, USA) at 8 weeks of age and grouped housed in same gender in OptiMice ventilated racks. Mice were acclimated to the vivarium for a week prior to injections. For neonatal injections, pregnant C57Bl6/J mice (E13 – E15) were purchased from The Jackson Laboratory. Mice were housed in OptiMice ventilated racks. Pups were weaned at 21 days and grouped housed by gender and treatment group. Over the course of the study, 12/12 light/dark cycles were maintained. The room temperature was maintained at 20-23 ºC with a relative humidity of around 50%. Chow and water were provided ad libitum.

On the day of cell grafting, media was aspirated from the T25 flasks with iPSC-derived astrocytes (day 30) and 2 ml of Accutase (room temperature) was added per flask and incubated for 7 min, after which the cells were monitored by microscopy every 2-3 minutes until rounding of the cells was observed. Astrocytes were then pooled in sterile conical tubes and centrifuged at 300 g at room temperature for 3 min. Cell pellets were gently resuspended in 1-5 ml DPBS. Cell numbers were counted with Countess Counter (Thermo Fisher Scientific) with Trypan Blue staining. Live cell numbers were calculated, and the cell suspension was supplemented with CEPT. After resuspension, cells were kept on ice. 3 μl of suspension (50.000 cells) per hemisphere was injected.

To perform intracerebroventricular (ICV) injections into newborn mice (postnatal day 1), animals were exposed to cryoanesthesia and injected with a dose volume of 1µl/g solution. A micro-liter calibrated sterilized glass micropipette was used that was attached to a 10 µl Hamilton syringe. The needle tip was adjusted to correct length for a 2 mm penetration into the skull. The immobilized mouse was firmly grasped by the skin behind the head. A fiber optic light was used to illuminate relevant anatomical structures for guidance. The needle was penetrated, perpendicularly, 2 mm into the skull, for ICV at a location approximately 0.25 mm lateral to the sagittal suture and 0.50-0.75 mm rostral to the neonatal coronary suture. Dosing solution was dispensed slowly (about 1µl/sec). Once the dose was administered, the needle was slowly removed (about 0.5 mm/sec) to prevent back flow.

For grafting into adult mice, animals were placed in an induction chamber to receive anesthesia using 2% isoflurane in the air mixture. The fur of the scalp and anterior back was clipped, and the animal was placed back into the induction chamber. The animal was then placed in a stereotactic apparatus such that the 180 ear bars were in the ear canals and the incisors were in the tooth bar of the mouse adapter. Surgical planes of anesthesia were maintained with 2% isoflurane by a nose cone fitted to the stereotaxic instrument. The scalp was prepared for surgery by cleaning the clipped injection site with Povidone iodine and rinsed with 70% ethanol. Mice were checked for a withdrawal reflex by pinching the hind foot to assess for anesthetic depth before an incision was made. A 1-1.5 cm slightly off-center incision was made in the scalp. The subcutaneous tissue and periosteum were scraped from the skull with sterile cotton tipped applicators. The guide cannula attached to stereotaxic arm was positioned over Bregma and this coordinate is considered the zero point. The guide cannula was moved to the appropriate anterior/posterior (-1.9) and medial/lateral (+/- 0.3) coordinates. Mice were infused with cells bilaterally in the cortex at a depth of (-2.5) with 3 ul on each side, at a rate of 0.3 µl/min with a 4 min rest period following injection. Overall, one adult mouse and 3 pups died post-injection.

For brain collection, animals were randomly split into two groups for collections at 2 time points after engraftment: 1) 4 weeks post grafting; 2) 8 weeks post grafting. Mice were deeply anesthetized with pentobarbital and monitored for loss of reflexes until all the responses to external stimuli cease (verified by a toe pinch). The abdominal cavity was opened, followed by opening of the chest cavity. A blunt-end perfusion needle was inserted into the left ventricle and forwarded toward the ascending aorta. Immediately after, a small incision was made

on the right atria. The perfusion needle was connected to an automated perfusion pump through a catheter system for a continuous administration of ambient temperature phosphate-buffered saline (PBS; 20 mM, pH 7.4 at room temperature). Approximately 40 ml of PBS was perfused at a rate of 10 ml/min. Saline flush was followed by perfusion with freshly prepared phosphate buffered 4% PFA. Brains were harvested and post-fixed overnight in freshly prepared phosphate buffered 4% PFA then transferred to 15% sucrose/PBS solution.

For immunohistochemistry, cryosectioned brains were stained to detect expression of human cytoplasmic marker STEM121 (TaKaRa, Y40410) and human-specific GFAP marker STEM123 (TaKaRa, Y40420). As general astrocyte markers GFAP (DAKO, z0334) and S100B (Abcam, ab52642) were used.

For quantitative image analysis, four different ROIs were manually drawn in Image J and either concentrated on the cerebral cortex around the graft injection site or delineated the entire hemisphere. A bilevel black and white DAPI mask was stored for every ROI and image. The inverted DAPI mask was mathematically subtracted from the S100B original image channel. A mask of $S100B^+$ nuclei was stored for each image and ROI. The mask of $S100B^+$ nuclei was mathematically added to the original S100B image. This procedure allowed for extraction of the entire shape of cells around the $DAPI^+$ and $S100B^+$ nucleus as far as labeled. This approach guaranteed that only structures that can be measured are those directly attached, hence, segmented processes were not included. A mask reflecting this core shape of $S100B^+$ astrocytes was saved for each image and ROI. The inverted S100B cell mask was subtracted from the original STEM123 image and signal above threshold and size restrictions overlapping with $S100B^+$ morphology was counted using restrictions and “fill holes” and “pixel connect” option to assure that for every IR area one object is counted (not to bias objects density). All cell transplantation experiments were performed by PsychoGenics (Paramus, NJ, USA) as part of a service agreement. The protocol was approved by the Committee on the Ethics of Animal Experiments of PsychoGenics and NIH.

Bulk RNA-seq

hPSCs and differentiating cells at different time points were lysed using buffer RLT+ (1053393, Qiagen) supplemented with 2-mercaptoethanol (63689, Millipore-Sigma) directly in wells and RNA was extracted and purified using RNeasy Plus Mini Kit (74136, Qiagen) according to the manufacturer’s instruction. QIAcube

automated workstation was used for the extraction (Qiagen). Genomic DNA was eliminated by both the gDNA eliminator column and on-column incubation with DNase I (79256, Qiagen). Sequencing libraries were constructed and sequenced using TruSeq® Stranded mRNA kit (20020597, Illumina) and NovaSeq 6000.

Bulk RNA-seq analysis

Samples were preprocessed with a standard pipeline that can be viewed at https://github.com/cemalley/Jovanovic_methods. Software used in preprocessing included fastqc 0.11.9, STAR 2.7.8a, trimmomatic 0.39, htseq 3.7.3 (http://www.bioinformatics.babraham.ac.uk/projects/fastqc) (Dobin et al., 2013), (Anders et al., 2015). Analysis was performed in R 4.0.3 (R Core Team 2021 https://www.R-project.org/). Samples were combined with RUVSeq batch correction method RUVg using a set of housekeeping genes (Risso et al., 2014), gene list (Wang et al., 2019).The UCSC Cell Browser cortex development dataset was mined to find unique differentially expressed genes among the radial glia cell subpopulations RGdiv1, oRG, or Pan-RG (https://cells.ucsc.edu/?ds=cortex-dev). DESeq2 was used to merge and normalize samples with the median-of-ratios method (Love et al., 2014). Normalized counts from the resulting R object were row Z-score transformed and scaled before plotting a subset of the DE RG genes, key pluripotency and astrocyte markers in a heatmap using ComplexHeatmap 2.6.2 (Gu et al., 2016). Several public RNA-Seq datasets were obtained from the Sequence Read Archive and merged with the day 30 and day 50 iPSC-astrocyte samples (Figure 4): PRJNA412090 or GSE104232 (Tchieu et al., 2019) (https://www.ncbi.nlm.nih.gov/bioproject/PRJNA412090); PRJNA382448 or GSE97619(Santos et al., 2017) (https://www.ncbi.nlm.nih.gov/bioproject/PRJNA382448); PRJNA383243 or GSE97904(Tcw et al., 2017) (https://www.ncbi.nlm.nih.gov/bioproject/PRJNA383243); and PRJNA297760 or GSE73721(Zhang *et al.*, 2016) (https://www.ncbi.nlm.nih.gov/bioproject/PRJNA297760). Merging was done with the same RUVSeq RUVg method as described previously. Principal component analysis plots were created in R with base function prcomp. Gene set enrichment was performed using the top 100 DE genes per contrast and input to Enrichr, querying the Gene Ontology 2019 or ARCHS4 Tissues databases. Regional marker genes were derived from a list of previously published genes showing significant differential gene expression across eight regions of the developing brains at Carnegie stage 22. (Eze et al., 2021). The ten most-significant genes (adjusted p-value) from each region were used to filter normalized count data from newly

generated time-course RNA-seq for astrocyte differentiation. Clustering of samples was performed with the dendsort R package, gene clustering and heatmap were produced with the pheatmap and viridis R packages (Figure S4).

ATAC-seq and MeDIP-seq analysis

Raw Data. ATAC-seq and MeDIP-seq experiments were performed by Active Motif (Carlsbad, CA, USA) and initial analyses provided included the following: 1. Sequencing and mapping paired-end Illumina sequencing reads to the reference human hg38 genome using BWA; 2. Alignment and peak calling statistics (using MACS2); 3. Generating summary statistics across samples comparisons; 4. Annotation of all intervals (peak regions); 5. Gene-centric rollup of the intervals table; 6. A top table comparing peak region metrics between different samples; 7. A UCSC custom tracks BED file; and 8. A signal map bigwig URL file for viewing in the UCSC viewer.

Modified differential peak analysis. Active Motif included all identified peaks in MACS2. To conservatively assess differential accessibility or methylation, only peaks supported by at least two biological replicates were retained for downstream analysis. DESeq-2 was then run on the filtered peaks (separately for ATAC-seq and MeDIP-seq) using default parameters.

For MeDIP-seq analysis reference genome for human hg38 was generated in BWA, paired-end fastq files aligned to the reference and counts generated using Rsubread with featureCounts (specifying paired-ends). DESeq2 was then used to normalize counts using the “median by ratios” method and used to run differential peak analysis for all pairwise comparisons (iPSC day 0 vs RGCs day 7; iPSC Day 0 vs astrocytes D30 and astrocytes D50; RGC Day 7 vs astrocytes D30 and astrocytes D50).

Overrepresentation analysis. After performing differential peak analysis, peaks were retained if their adjusted p-value was less than 0.05, the peaks ranked by adjusted p-value and overrepresentation analysis was performed using all Gene Ontology (GO) gene sets and Kyoto Encyclopedia of Genes and Genomes (KEGG) 2019 with the R library, clusterProfiler using Benjamini Hochberg correction and an adjusted p-value cut-off of 0.01.

Principal Component Analysis (PCA). For ATAC-seq and MeDIP-seq data, PCA was performed to determine each peak’s variability across samples and genome-wide. The purpose behind performing this analysis was to determine which peak drives the variance across a given gene locus. For some gene loci, there were several

identified ATAC-seq and MeDIP-seq peaks; however, it was not clear which peak might be driving differential accessibility or methylation. To perform this analysis, normalized count data was used in the prcomp function in R to perform PCA. For each gene, the peak with the largest variance was extracted from the PCA. Only peaks within 1,000 base pairs of an annotated gene were included in this analysis (which excludes enhancer elements that are far up-or downstream of a given gene).

The pre-filtered peak per gene with the highest variance was used to build dot plots for a targeted list of genes. All samples and normalized counts were used to calculate the interquartile range (IQR) for each gene (peak), separately. For each gene, peak and sample, the normalized count data was specified by the following criterion: 1. The median of the normalized counts was less than 0.25 quartile: Inaccessible (hypo-methylated); 2. The median of the normalized counts was greater than 0.75 quartile: Hyper-accessible (hyper-methylated); or 3. The median of the normalized counts was between 0.25 and 0.75 quartiles: Mid-accessible (mid-methylated). The above criterion was used to generate the dot plots shown in Figures 5D and 5G.

Single-cell RNA sequencing

Cryopreserved vials of single cell suspensions (1Mio. cells/ml) of hESC-Astrocytes, iCell Astrocytes and iGluta neurons were sent to GENEWIZ for single cell RNA sequencing. Samples were submitted in technical duplicates with a minimum of ≥90% viability post thaw. Additionally, to assist with samples that are submitted with ≤90% viability post thaw, GENEWIZ has implemented a dead cell removal workflow to enhance sample viability.

For single cell RNA-sequencing, 10X Genomics Chromium platform was used. After the library preparations, samples were sequenced on the Illumina HiSeq4000 in a 2x150bp fashion.

Single-cell RNA sequencing data analysis

BCL files produced by the Illumina sequencer were converted to FASTQ files using command mkfastq from theCellRangeranalysis toolkit (10X Genomics, v. 3.1.0,). The FASTQ files were processed with CellRanger count to produce count matrices suitable for analysis in R using package Seurat1(v. 4.0.3).Identification of clusters was performed in Seurat using the Leiden algorithm2(argument “algorithm=4”) at a resolution of 0.4. Pseudotime trajectory analysis was performed using slingshot (Street et al., 2018) and the analysis of the

dynamics of gene expression relative to the previously identified trajectories was performed using tradeSeq (Van den Berge et al., 2020). Integration with external data for the purpose of UMAP visualization was performed using Seurat. Gene set enrichment analysis was performed in R using Enrichr (package “enrichR”). All plots were constructed using ggplot28.The analysis scripts are available at https://github.com/jaro-slamecka/Jovanovic_astrocyte_scRNA-seq.

References

Anders, S., Pyl, P.T., and Huber, W. (2015). HTSeq--a Python framework to work with high-throughput sequencing data. Bioinformatics *31*, 166-169. 10.1093/bioinformatics/btu638.

Dobin, A., Davis, C.A., Schlesinger, F., Drenkow, J., Zaleski, C., Jha, S., Batut, P., Chaisson, M., and Gingeras, T.R. (2013). STAR: ultrafast universal RNA-seq aligner. Bioinformatics *29*, 15-21. 10.1093/bioinformatics/bts635.

Gu, Z., Eils, R., and Schlesner, M. (2016). Complex heatmaps reveal patterns and correlations in multidimensional genomic data. Bioinformatics *32*, 2847-2849. 10.1093/bioinformatics/btw313.

Love, M.I., Huber, W., and Anders, S. (2014). Moderated estimation of fold change and dispersion for RNA-seq data with DESeq2. Genome Biol *15*, 550. 10.1186/s13059-014-0550-8.

Risso, D., Ngai, J., Speed, T.P., and Dudoit, S. (2014). Normalization of RNA-seq data using factor analysis of control genes or samples. Nature Biotechnology *32*, 896-902. 10.1038/nbt.2931.

Tristan, C.A., Ormanoglu, P., Slamecka, J., Malley, C., Chu, P.H., Jovanovic, V.M., Gedik, Y., Jethmalani, Y., Bonney, C., Barnaeva, E., et al. (2021). Robotic high-throughput biomanufacturing and functional differentiation of human pluripotent stem cells. Stem Cell Reports *16*, 3076-3092. 10.1016/j.stemcr.2021.11.004.

Wang, Z., Lyu, Z., Pan, L., Zeng, G., and Randhawa, P. (2019). Defining housekeeping genes suitable for RNA-seq analysis of the human allograft kidney biopsy tissue. BMC Med Genomics *12*, 86. 10.1186/s12920-019-0538-z.